Applied Ocean Research 138 (2023) 103588

Contents lists available at ScienceDirect

Applied Ocean Research

journal homepage: www.elsevier.com/locate/apor

Experimental study of floating bridge global response when subjected to waves and current

Thomas Viuff [a,*], Senthuran Ravinthrakumar [a], Ole David Økland [a], Ole Anton Grytå [b], Xu Xiang [b]

[a] SINTEF Ocean AS, Trondheim, N-7465, Norway
[b] Norwegian Public Roads Administration (NPRA), Oslo, N-0667, Norway

ARTICLE INFO

Keywords:
Hydroelastic behaviour
Wave–current interaction
Long-crested waves
Hydrodynamic interaction
Extreme response

ABSTRACT

The present paper investigates the wave- and current-induced responses of the Bjørnafjord phase 5 K12 floating bridge concept based on small-scale model tests. Due to the extensive length of the bridge concept combined with relatively small wave heights governing the design, the experimental model represents a truncated section of the original bridge concept. This truncated section includes a stay-cable tower and ten floating pontoons supporting a horizontally curved bridge girder at varying altitude. The bridge girder truncation points coincide with the tower column and the location just above the first moored pontoon. The girder boundary conditions are simplified as fixed for all degrees of freedom (DOF) on either side of the model while allowing for free rotation around the longitudinal and vertical axes at the location above the otherwise moored pontoon. The instrumentation of the experimental model includes three DOF translational motions captured at 13 locations along the bridge and six DOF motion of each pontoon. Force transducers are used to capture axial forces in all ten tower stay-cables and at the two ends of the bridge girder, while strain gauges capture shear forces and bending- and torsional moments measured at 12 locations along the bridge girder.

The dynamic properties of the model are investigated by subjecting the model to both regular waves and broad-banded, long-crested waves, propagating at two different wave directions corresponding to waves travelling in and out of the fjord. These tests are performed with and without collinear current to investigate the effect of current on the bridge responses. Subsequently, the effect of current is investigated for two important long-crested wave conditions, i.e. the 100-year wind wave condition and the 10000-year swell wave condition. For both wave conditions the model tests are performed without current and with 1-year and 10-year current velocities, respectively. Finally, the short-term response from the long-crested wind and swell wave conditions without current are compared to those of short-crested waves without current.

Results show that both current and the directional distribution of the waves have a significant influence on the structural responses. It is recommended that both effects are properly accounted for in any future design.

1. Introduction

Design of floating bridges has long been an interest within offshore and coastal engineering and has once again become a relevant topic as the Norwegian Public Roads Administration (NPRA) is planning to build very long (roughly 5,000 m) floating bridges as viable solutions to crossing the many deep and wide fjords in the western part of the country (Watanabe, 2003; Moan and Eidem, 2020; Viuff, 2020). Many aspects must be considered in the design, and special studies such as hydrodynamic damping at the pontoons (Xiang et al., 2017; Baarholm, 2017; Shao et al., 2019; Ravinthrakumar et al., 2023), wave–current interaction effects (Løken et al., 1990; Xiang and Løken, 2019; Viuff et al., 2020; Dai et al., 2022; Fenerci et al., 2022), hydrodynamic interaction between pontoons (Xiang et al., 2018; Xiang and Løken, 2019) and inhomogeneous wave fields (Cheng et al., 2018, 2019; Dai et al., 2020; Rodrigues et al., 2020) have received increasing interest in recent years. During the same period, several iterations of the proposed floating bridge concepts have been performed by the various engineering consortia contracted by the NPRA, resulting in the recent Bjørnafjord phase 5 concept (AMC, 2019).

Previous experimental studies on floating bridges include a generic, curved pontoon bridge (Aarsnes et al., 1990a,b) in 1990, which has been compared to numerical studies (Løken et al., 1990; Xiang and Løken, 2019; Viuff et al., 2020; Dai et al., 2022) in order to investigate hydrodynamic interaction (Xiang and Løken, 2019) and wave–current interaction (Xiang and Løken, 2019; Viuff et al., 2020; Dai et al., 2022),

* Corresponding author.
E-mail address: thomas.viuff@sintef.no (T. Viuff).

https://doi.org/10.1016/j.apor.2023.103588
Received 19 December 2022; Received in revised form 17 March 2023; Accepted 1 May 2023
Available online 9 June 2023

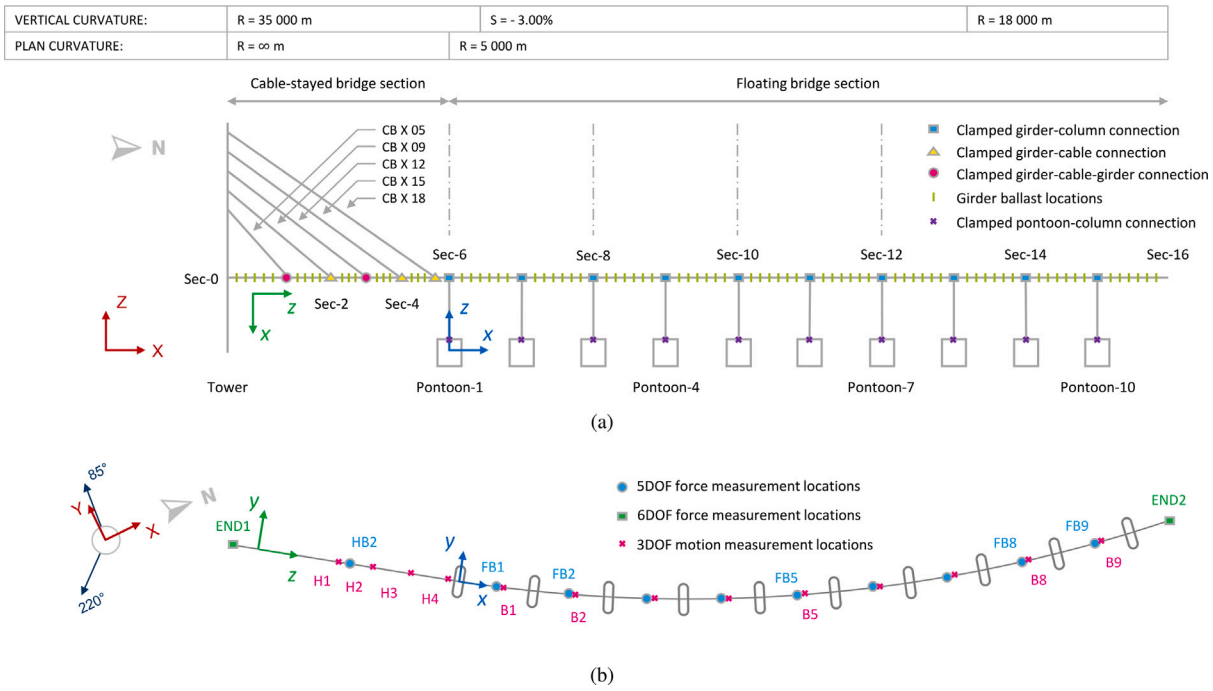

Fig. 1. Diagram of floating bridge model with relevant nomenclature and coordinate systems. (a) View from East, perpendicular to the roadline. The 'X' in the stay-cable name convention refer to EAST and WEST for stay-cables on either side of the bridge girder. (b) View from above. Measurements at the bridge girder are indicated along the bridge, as well as *going towards* wave directions of the performed wave tests. Illustration is a modified version of the one in Viuff et al. (2023).

of which Xiang and Løken (2019) and Viuff et al. (2020) included the effect of current on the first order wave loads only. Later on Dai et al. (2022) extended the comparison by also including the current effect on the radiation properties of the pontoons and found an improved fit to the experimental results. More recently Rodrigues et al. (2020, 2022) described an experimental study of a very long, straight pontoon bridge. Due to the extensive length of the bridge, a truncated section of the prototype is modelled in the Ocean Basin, where the two truncation points coincide with moored pontoons, which are included in the experimental model. A thorough description of the experimental model and the procedure leading up to the model design is given in Rodrigues et al. (2022), including a discussion of the truncation method used. A recent experimental study related to the Bjørnafjord phase 5 concept (Ravinthrakumar et al., 2023) investigated the effect of current and hydrodynamic interaction between the pontoons. The tests included: (i) forced oscillation tests of a single pontoon moving transverse to the bridge longitudinal axis; (ii) combinations of wave and current tests for a single pontoon with fixed and flexible boundary conditions; and (iii) combinations of wave and current tests for three adjacent pontoons where the two outer most pontoons are fixed and the middle pontoon has both fixed and flexible boundary conditions.

Although previous studies have been performed on the current and wave response for floating bridges, see e.g. Xiang and Løken (2019), Viuff et al. (2020), Dai et al. (2022), the conclusions as to the effect of current on the wave-induced responses is still not clear and relevant experimental data is scarce. The present paper is an experimental study on the wave- and current responses of a truncated section of the Bjørnafjord phase 5 concept and is a continuation of Viuff et al. (2023), where the experimental model and relevant research carried out prior to this study is described in detail. The methods used in building the experimental model in the present study is heavily influenced by the above listed research and in particular the recommendations and thoughts given in Rodrigues et al. (2022).

2. Brief description of the model setup

The floating bridge model described in the present paper is based on the phase 5 Bjørnafjord floating bridge concept (AMC, 2019) and only represents a specific section of the full bridge as specified in Xiang and Løken (2020), i.e. the section from the cable-stayed tower, including the front span cables, the curved bridge girder and the first ten supporting pontoon columns and pontoons to the point just above the first moored pontoon, excluding the moored pontoon itself and the corresponding pontoon column. The truncation points are chosen at these locations as they are considered natural boundary conditions for the experimental model. A detailed description of the experimental model is given in Viuff et al. (2023). This includes specifics on the curved bridge geometry, stiffness and mass properties of the various structural parts, measurement accuracy and a comprehensive list of instrumentation and tests performed. In the present study, a brief description is provided for an overview of the model and the reader is otherwise referred to Viuff et al. (2023) for more information about the experiment and to AMC (2019) regarding the concept in general.

An overview of the geometry and nomenclature is given in Fig. 1. The bridge girder is 1630 m in full scale along the curved girder roadline. The double-symmetric bridge girder is curved in both the horizontal- and vertical plane and supported by a tower in one end and floating pontoons at the other. Sec-0 in Fig. 1 indicates the starting point of the bridge girder at the tower, also referred to as END1. From Sec-0, the girder stretches along the cable-stayed bridge section where the girder is supported by five sets of two stay-cables connecting to the bridge girder at Sec-1 to 5, respectively. The girder then stretches further into the floating bridge section, starting at Sec-6, where the bridge is supported by 10 geometrically identical 'circtangular' shaped pontoons, equidistantly distributed between Sec-6 and Sec-15 with 125 m in between. Finally the bridge girder ends at Sec-16, also referred to as END2, which is the point just above the otherwise first moored pontoon. Each pontoon is oriented with the pontoon longitudinal axes perpendicular to the bridge girder axis and is connected to the bridge girder via a single circular shaped column. The mass per metre and stiffness properties of the 10 columns are almost identical, but the column length varies roughly between 13–46 m due to the vertical curvature of the bridge girder. This elevation starts at the lowest point at Sec-16 roughly 17 m above the still water level (SWL), to roughly 60 m at Sec-0 following the curvature listed in Fig. 1. The bridge girder

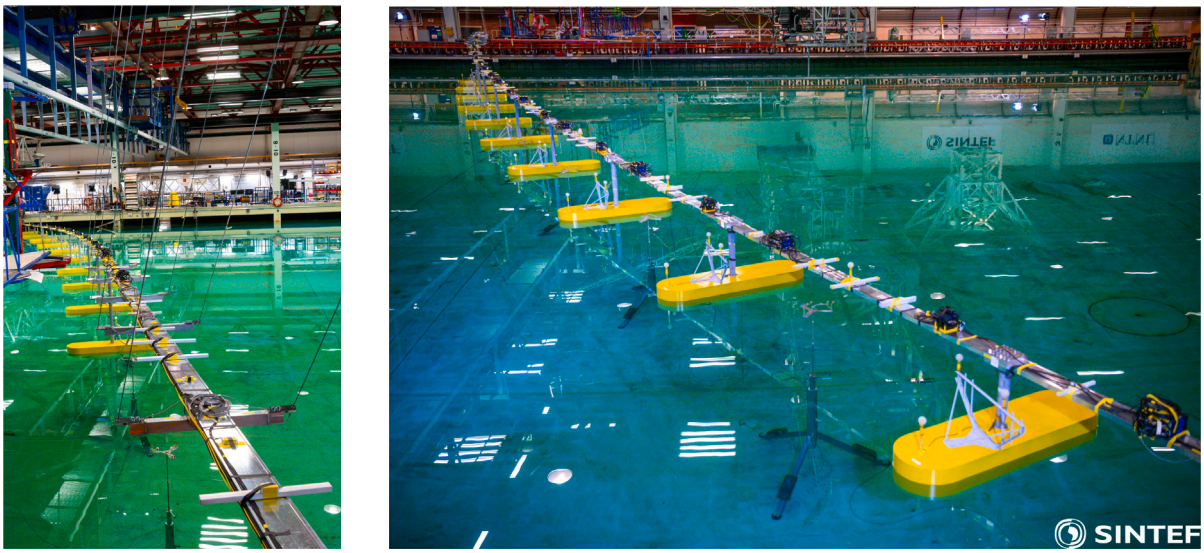

(a) (b)

Fig. 2. Photos of build model in the Ocean Basin. (a) View from END1. (b) View from END2 (Viuff et al., 2023).

consists of multiple curved girder elements, connected to each other and to the cables and pontoon columns via stiff clamped connections, which for all practical purposes are considered as rigid.

The supporting pontoons all have the same outer dimensions with a length of 53 m, a width of 14.9 m, a draft of 5 m and a freeboard of 3.5 m and each have a unique yaw rotation about their local z axis in accordance with the horizontal curvature of the bridge girder.

The mass of the ten pontoons is governed by the vertical static equilibrium between the bridge gravitational and buoyancy forces, and so, with the exception of Pontoons-1, 2 and 3 influenced by the tower cables, the mass of the pontoons decreases slightly going from Sec-16 to Sec-0. The radius of gyration values of all pontoons are roughly the same, except for small deviations for Pontoon-1. The mass of Pontoon-1 is almost twice the average value of the other pontoons while the mass of Pontoon-2 is roughly three fourths. The resulting overturning moment at the bridge girder is compensated by adjusting the pre-tension in the adjacent tower stay-cables.

At Sec-0, the bridge girder is supported by a rigid tower via 10 pre-tensioned cables (one at each side of the bridge girder) at Sec-1 to Sec-5 at a distance $y = \pm 14$ m in the local bridge girder coordinate system measured from the girder neutral axis. The tower is roughly 220 m high and the length of the cables is approximately 133–393 m. Each cable consists of a long steel rod for most of the length with a short axial spring at the top and a connecting force transducer at the bottom. The mass per metre of each cable is identical for all practical purposes, while the total axial stiffness of each set of cables, representing the entire cable length, is highest at the inner most cable set and decrease towards the outer most cable set.

The geometry of the truncated floating bridge model is thoroughly described in Viuff et al. (2023). The global $OXYZ$ coordinate system, cf. Fig. 1, with origin at the SWL is used to describe the location of the various bridge elements, the wave- and current directions, as well as the bridge girder local $oxyz$ coordinate system with origin at the neutral axis and the z-axis following the continuous tangent of the bridge girder. Each pontoon and pontoon column utilize a local $oxyz$ coordinate system with origin at the SWL, with the local y-axis along the pontoon longitudinal axis and the local z-axis pointing upwards along the column axis.

At Sec-0 the bridge girder is fixed in all degrees of freedom (DOFs), while at Sec-16 it is fixed in all DOFs except for translation along the local z-axis and rotation around the local z and x axes, corresponding to girder axial motion, torsional motion and strong axis (horizontal) bending, respectively. The torsional and strong axis bending motion are modelled as free, while a slightly non-linear spring is acting in the axial direction to compensate for a relatively large axial stiffness of the bridge girder as a consequence of scaling priorities focusing on weak and strong axis bending properties and robust strain gauge measurements.

Photos of the final build model is presented in Fig. 2, taken from the edges of the Ocean Basin facility looking along the bridge from each end.

2.1. Waterdepth and model scale

The floating bridge model is constructed in scale 1:31 using Froude similarity and all results presented refer to full scale, unless otherwise specified. Due to the need for relatively strong current velocities in the test facility, the water depth had to be reduced from the 350–500 m reported in AMC (2019) to 77.5 m as specified in Xiang and Løken (2020).

2.2. Structural modes and natural periods captured from decay tests

Due to the curved geometry of the bridge girder, the first two (horizontal) modes of the structure have shapes similar to a single sine wave along the length of the bridge, with two different locations of the zero-deflection point. Both modes include significant torsional motion of the bridge girder. The natural period of the first and second mode is 15.1 s and 13.7 s, respectively. These natural periods are estimated from decay tests and obtained from Viuff et al. (2023).

2.3. Overview of measured responses

The bridge model is heavily instrumented in order to obtain both motion and force responses throughout the bridge. The entire list of instrumentation is given in Viuff et al. (2023) and only the most relevant measurements are listed below:

- Wave elevation and current velocity at the centre of the Ocean Basin.
- Six DOF motion of each pontoon, a total of 60 measured responses.
- Three DOF translational motion of bridge girder at 13 locations along the main span, a total of 39 measured responses.

Table 1
Location of reference points for the MoCap measurements along the bridge girder roadline, relative to Sec-0 (Viuff et al., 2023). The actual diodes are positioned at a slight distance relative to the bridge girder neutral axis. This distance x refers to distance along the direction of the x axis in the local bridge girder coordinate system. The diodes H1, H2, H3 and H4 are located at x values of 4.898 m, 4.495 m, 4.774 m and 4.619 m, respectively, while all the diodes starting with B are located at $x = -5.115$ m and at an offset $z = 7.13$ m from the actual midspan. The X, Y and Z notations used in the measurement notation refer to the translational motion along the local bridge girder coordinate system.

Location ID	Roadline (m)	Measurements (m)	Position close to
H1	182.20	HX1, HY1, HZ1	Sec-2
H2	243.70	HX2, HY2, HZ2	Sec-3
H3	302.30	HX3, HY3, HZ3	Sec-4
H4	368.40	HX4, HY4, HZ4	Sec-5
B1	449.50	BX1 2, BY1 2, BZ1 2	Sec-6 and Sec-7 midspan
B2	574.50	BX2 3, BY2 3, BZ2 3	Sec-7 and Sec-8 midspan
B3	699.50	BX3 4, BY3 4, BZ3 4	Sec-8 and Sec-9 midspan
B4	824.50	BX4 5, BY4 5, BZ4 5	Sec-9 and Sec-10 midspan
B5	949.50	BX5 6, BY5 6, BZ5 6	Sec-10 and Sec-11 midspan
B6	1074.50	BX6 7, BY6 7, BZ6 7	Sec-11 and Sec-12 midspan
B7	1199.50	BX7 8, BY7 8, BZ7 8	Sec-12 and Sec-13 midspan
B8	1324.50	BX8 9, BY8 9, BZ8 9	Sec-13 and Sec-14 midspan
B9	1449.50	BX9 10, BY9 10, BZ9 10	Sec-14 and Sec-15 midspan

- Six DOF loads at the bridge girder ends, a total of 12 measured responses.
- Five DOF loads (no axial force) at 11 bridge girder mid-spans, a total of 55 measured responses.
- Axial load in the stay-cables at the lower ends, a total of 10 measured responses.

The wave elevation captured at the centre of the Ocean Basin is used as the reference wave when describing response amplitude operators (RAOs).

The motion response is obtained via an optical-electronic motion capture system (MoCap), using a single light diode for three DOF translational motion of the bridge girder and three diodes for six DOF motion of each pontoon, see Fig. 2. The location of the MoCap measurement reference points along the bridge girder is listed in Table 1 and indicated in Fig. 1(b).

The six DOF pontoon motions are also referred to as XPOS, YPOS, ZPOS, PITCH, ROLL and YAW, referring to translational motion along the local pontoon x, y and z axes and angular motion around the same axes, respectively.

Strain gauges are used to capture the shear forces FX and FY, torsional moment MZ and bending moments MX and MY in the bridge girder and at the two ends, see Tables 2 and 1(b) for the locations and name convention used for the responses. The axial force at Sec-0 is captured via a force transducer and the axial force at Sec-16 is captured by converting measured displacements to axial force via a known non-linear force–displacement relationship of the axial spring.

The cable axial forces are captured using force transducers at the lower ends of the cables, connected to the bridge girder. The measured forces include both static and dynamic values, where the static axial forces are measured during calm water conditions prior to the tests. Before each test, the force measurement is zeroed in order to measure only the dynamic response. The static values are added to the dynamic measurements to have the final axial tension values during post-processing.

All measurements during the tests are synchronized and sampled at 200 Hz (model scale). All gauges and sensors are calibrated prior to the model assembly in the Ocean Basin.

2.4. Wave- and current tests

The test program is performed in three phases: (i) calibration of environmental loads such as waves and current; (ii) documentation tests of the build model such as static pull-out tests, decay tests and pure current tests; and (iii) tests of bridge response under wave- and current loads. Phases i and ii are described in Viuff et al. (2023) and the present study focuses on the bridge responses during phase iii.

Table 2
Location of measurement positions for forces (FX, FY, FZ) and moments (MX, MY, MZ) in the bridge girder following local bridge girder coordinate system (Viuff et al., 2023). Position is given as distance along the roadline relative to Sec-0.

Location ID	Roadline (m)	Measurements (N) or (Nm)	Description
END1	0.00	FX, FY, FZ, MX, MY, MZ	Sec-0
HB2	192.39	FX, FY, MX, MY, MZ	Sec-0 and Sec-6 midspan
FB1	442.50	FX, FY, MX, MY, MZ	Sec-6 and Sec-7 midspan
FB2	567.50	FX, FY, MX, MY, MZ	Sec-7 and Sec-8 midspan
FB3	692.50	FX, FY, MX, MY, MZ	Sec-8 and Sec-9 midspan
FB4	817.50	FX, FY, MX, MY, MZ	Sec-9 and Sec-10 midspan
FB5	942.50	FX, FY, MX, MY, MZ	Sec-10 and Sec-11 midspan
FB6	1067.50	FX, FY, MX, MY, MZ	Sec-11 and Sec-12 midspan
FB7	1192.50	FX, FY, MX, MY, MZ	Sec-12 and Sec-13 midspan
FB8	1317.50	FX, FY, MX, MY, MZ	Sec-13 and Sec-14 midspan
FB9	1442.50	FX, FY, MX, MY, MZ	Sec-14 and Sec-15 midspan
END2	1630.00	FX, FY, FZ, MX, MY, MZ	Sec-16

The wave and current responses are investigated for two different wave directions specified as the *going towards* directions 85 and 220 degree from North, cf. Fig. 1. The wave tests involve both regular and irregular waves with and without current. The specified regular wave period varies from 4.0 s to 18.0 s with a wave height of 1.0 m for most waves. The wave periods in the range 4.0–11.0 s had an interval of 0.2 s, while the wave periods from 11.0 s and up had an interval of 0.5 s. Two extra 1.0 m regular waves were tested with wave periods at 13.8 s and 14.2 s.

Long-crested, irregular waves were also performed, both with and without current. These include broad-banded waves with a significant wave height of 1 m and with wave energy between 3.5–20.0 s. A few long-crested irregular waves governed by the three-parameter JONSWAP wave spectrum are tested with and without current. The performed tests are based on varying significant wave heights (H_s), peak periods (T_p), peak enhancement factors (γ), spreading exponents (s) using the $\cos^s$ spreading function, wave directions (θ) and current velocities (U_c), cf. Table 3.

Finally, short-crested wave without current are performed in order to observe changes in the response from the directional distribution in the waves.

For the tests with and without collinear current, the measured waves are calibrated towards a target wave spectrum based on the wave encounter frequency. An example of this is shown in Fig. 3.

The choice of current velocity and wind and swell wave conditions is based on information from Statens vegvesen (2018, Tables 1, 2 and 16) and the selected design load cases for the 100-year wind waves listed in AMC (2019, Table 10-2). The *going towards* directions 85 and 220 degree angles from North are equivalent to the [75–105] and [315–345] *coming from* wave sectors in the MetOcean Design basis (Statens vegvesen, 2018, Table 1), respectively. Furthermore, waves only response screening analyses in the frequency domain performed by the AMC consortium, lists three out of four 100-year wind wave design load cases for wave directions within these two wave sectors, cf. AMC (2019, Table 10-2), with wave parameters equal to or close to $H_s = 2.1$ m and $T_p = 5.5$ s. According to Statens vegvesen (2018), the significant wave height for the swell wave condition is equivalent to a 10000-year return period, whereas the choice of peak period is valid as long as it is between 12 and 20 s. For our purpose, the peak period is chosen so as to excite the first two natural periods of the model. The peak enhancement factors are based on the average of the suggested value ranges in Statens vegvesen (2018). Finally, the two current velocities correspond to the current levels with a return period of one and 10 years, respectively, at a depth of 1.5 m, cf. Statens vegvesen (2018, Table 16).

Table 3
Irregular wave tests conducted in the Ocean Basin with collinear current directions. For broad-banded waves, the T_p values indicate the period range.

Spectrum type	Return period (yrs)		θ	U_c	H_s	T_p	γ	s
	Wave	Current	(deg)	(m/s)	(m)	(s)	(–)	(–)
Broad-banded	–	–	85	0.00	1.00	3.5–20.0	–	–
Broad-banded	–	1	85	1.00	1.00	3.5–20.0	–	–
Broad-banded	–	–	85	0.00	2.00	3.5–20.0	–	–
Broad-banded	–	–	220	0.00	1.00	3.5–20.0	–	–
Broad-banded	–	1	220	1.00	1.00	3.5–20.0	–	–
Broad-banded	–	–	220	0.00	2.00	3.5–20.0	–	–
JONSWAP wind[a]	100	–	220	0.00	2.10	5.5	2	–
JONSWAP wind	100	1	220	1.00	2.10	5.5	2	–
JONSWAP wind	100	10	220	1.44	2.10	5.5	2	–
JONSWAP wind	100	–	220	0.00	2.10	5.5	2	4
JONSWAP swell	10 000	–	220	0.00	0.46	13.8	4	–
JONSWAP swell	10 000	1	220	1.00	0.46	13.8	4	–
JONSWAP swell	10 000	–	220	0.00	0.46	13.8	4	10

[a]Test performed 10 times with different wave seed numbers.

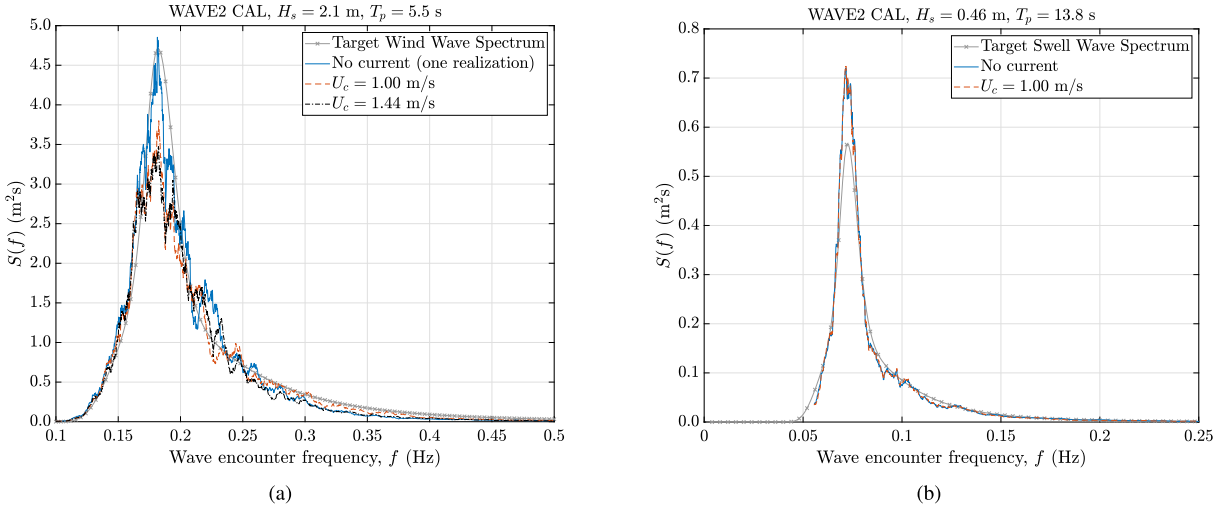

Fig. 3. Calibrated wave spectra towards target JONSWAP wave spectra for given wave encounter frequencies with and without current. (a) 100-year wind waves. (b) 10000-year swell waves.

2.4.1. Test duration

The duration of the regular wave tests was determined based on preliminary analyses, where it was observed that the bridge model required some time before reaching steady-state. For the regular waves with wave period $T < 7.0$ s, the duration of the regular wave test was 6 min (model scale). For the regular wave tests with $T \geq 7.0$ s, the duration of the regular wave tests was 12 min (model scale).

The duration of the irregular wave tests was chosen as 3 h (+ 40 min) in full scale. As argued above for the regular wave tests, the bridge model needs some time to reach steady-state. Hence, the first 40 min of the measured timeseries is removed during post-processing.

All measured currents and regular and irregular waves were calibrated towards specified values prior to the tests in the Ocean Basin. The current values are reported as time-averaged current velocities over a period of roughly 3 h and 15 min.

3. Supporting numerical calculations

As part of quality assurance and to support design choices in creating the physical experimental model, supporting numerical simulations are performed in the coupled, hydro-elastic SIMO-RIFLEX (SINTEF Ocean, 2021b,a) software. RIFLEX solves the static and dynamic equilibrium equations based on a non-linear Finite Element formulation allowing for large displacements (SINTEF Ocean, 2021a) and the hydrodynamic loads on the pontoons are received from SIMO, which generates the wave field and calculates the loads assuming the pontoons as large rigid bodies (SINTEF Ocean, 2021b). A representation of the numerical model is presented in Fig. 4.

The numerical model represents the as build properties of the experimental model and details can be found in Viuff et al. (2023). The hydrodynamic loads include first order diffraction and radiation loads from potential theory and mean drift loads based on Newman's approximation (Faltinsen, 1990). The numerical model approximates the hydrodynamic viscous loads at the pontoons using Morison's equation (Morison et al., 1950) with drag coefficients $C_{d,x} = 1.0$, $C_{d,y} = 0.5$ and $C_{d,z} = 4.8$ according to DNV (2010) for directions along the respective transverse, longitudinal and vertical pontoon axes. Structural damping is modelled as Rayleigh damping with a damping ratio $0.0004 \leq \xi_{struc} \leq 0.0008$ within the wave frequency range, based on structural damping level found in Viuff et al. (2023).

From the numerical model the natural frequencies and corresponding modeshapes are calculated. Generally, the procedure use to solve the eigenvalue problem is accounting for the added mass of the pontoons uses the added mass at infinite frequency. However, by performing a manually iteration it is possible to include the frequency-dependent added mass in the solution procedure, resulting in the results shown in Table 4 and Fig. 5. These results will be used to analyse the RAOs found experimentally from the model tests. From the modeshapes depicted in Fig. 5 it is clear that the many modes are a complex combination of both horizontal, vertical and torsional motion

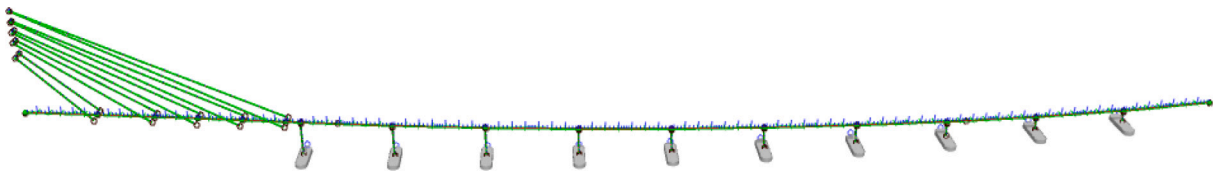

Fig. 4. Numerical SIMO-RIFLEX model used as part of quality assurance when building the physical model.

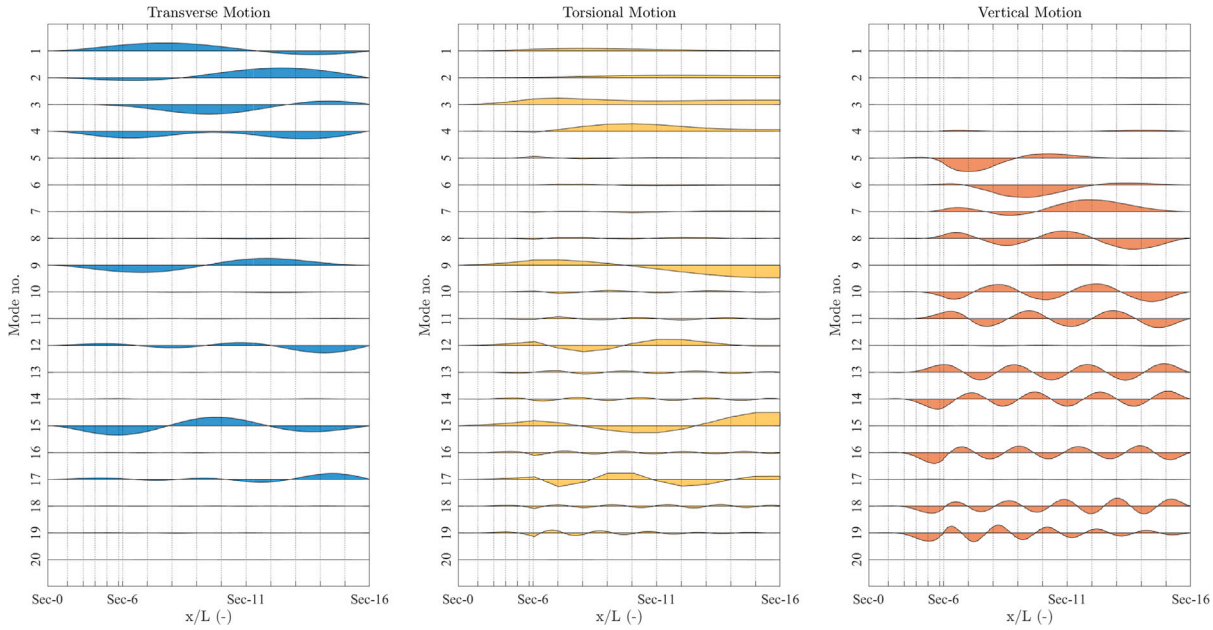

Fig. 5. Transverse, torsional and vertical modeshapes of the bridge girder, calculated from the numerical model. See Table 4 for the corresponding natural frequencies.

to various degrees. Although difficult to see in the depiction, even the first modeshapes have significant vertical motion close to the tower.

The results discussed in the following section are supported with results obtained from simulated regular wave responses. It should be mentioned that the numerical model is only used for simulating waves only responses and does not include any hydrodynamic interaction between the pontoons, although this effect was found to have a significant effect on the vertical bridge responses (Xiang et al., 2018; Fenerci et al., 2022). The calculated structural responses, using the numerical model, purely serve as reference values for the measured responses as part of the quality assurance of the performed tests and are referred to as 'NUM' in the figure legends.

4. Results and discussion

4.1. Response amplitude operators for waves propagating transverse to the bridge longitudinal axis

Two aspects are important to consider while calculating the first-harmonic steady-state RAOs from the model tests: (i) determining a steady state time-window; and (ii) filter the measured data around the wave period. By that, we present the first harmonic steady-state RAOs. The chosen time window is just after steady-state is reached. The filtering in ii is performed by bandpass filtering the measured data in the interval $0.8f$ and $1.2f$, where f is the wave frequency of the incident regular wave. An example of the measured and filtered response after steady-state responses are reached is presented in Fig. 6. We present the first-harmonic steady-state responses since the higher order responses are, in general, insignificant.

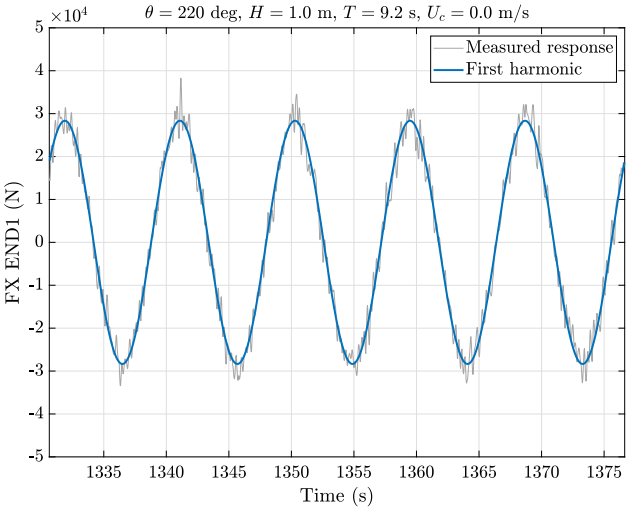

Fig. 6. Filtering of girder vertical shear force timeseries at END1 after steady-state response is reached. The filtered first-harmonic response is used for estimating the RAO at this particular regular wave period.

4.1.1. Wave response for waves propagating out of the fjord at 85 degrees without current

The horizontal motion of the bridge is to a large extent governed by the first two structural modes, with corresponding modeshapes similar to a single sine wave. With waves propagating at an 85 degree angle from North, this is close to perpendicular to the bridge longitudinal axis and the horizontal motion is expected to be strongly excited by the

Table 4
Natural frequencies of numerical model with as-build properties, taking into account the frequency-dependent added mass of the pontoons via a manual iteration procedure. All structural modes are a combination of horizontal (H), vertical (V) and torsional (T) motion of the bridge girder. For comparison, the natural periods of the first two modes of the as-build model are reported by Viuff et al. (2023) as 15.13 s and 13.67 s, respectively.

n (–)	T_n (s)	f_n (Hz)	ω_n (rad/s)	Dominant motion	n (–)	T_n (s)	f_n (Hz)	ω_n (rad/s)	Dominant motion
1	15.119	0.066	0.416	H	11	5.454	0.183	1.152	V
2	13.473	0.074	0.466	H	12	5.084	0.197	1.236	T
3	8.466	0.118	0.742	H	13	4.866	0.206	1.291	V
4	7.332	0.136	0.857	H	14	4.322	0.231	1.454	V
5	6.660	0.150	0.943	V	15	4.169	0.240	1.507	T
6	6.530	0.153	0.962	V	16	3.901	0.256	1.611	V
7	6.493	0.154	0.968	V	17	3.680	0.272	1.707	T
8	6.345	0.158	0.990	V	18	3.537	0.283	1.776	V
9	6.201	0.161	1.013	T	19	3.181	0.314	1.975	V
10	5.984	0.167	1.050	V	20	3.148	0.318	1.996	–

incident waves. Fig. 7 depicts the first harmonic horizontal motion and corresponding strong axis bending moment and torsional moment along the bridge girder when subjected to two regular waves at 85 degrees without current. The two regular waves have wave periods of 15.5 s and 13.5 s, which are close to the first and second structural mode, respectively. The responses are presented at a time instance where the maximum bridge girder transverse motion response occur within a steady-state time window. Although not indicated in the figure, all measurement locations are simultaneously at their maxima, except for the locations 1100 m or further away from Sec-0 along the bridge girder roadline. Here there is a slight phase shift, which could be due to a coupling between the horizontal and torsional motion of the bridge. Other possible reasons could be that the mode is damped by the potential and viscous damping at the pontoons or that the phase lag stems from the pontoon inertia forces. The regular wave response in Fig. 7(a) is very similar to the measured transverse motion from decay tests prior to the wave tests, described in Viuff et al. (2023) and dominated by the first mode at 15.1 second. Furthermore, the pontoon motion exceeds the girder motion, which indicates that there is a significant torsional motion associated with the first mode. This is also reflected in the torsional moment MZ along the bridge girder, shown in Fig. 7(c). It is noted that both the strong axis bending moment and the torsional moment at Sec-16 are zero and thereby verifying that the modelled boundary condition is free to rotate around the local bridge girder x and z axes. With this fundamental understanding of the horizontal motion along the bridge, we can readily obtain more detailed information regarding the dynamic response in frequency domain by investigating the RAOs of various selected responses along the bridge. RAOs of the transverse motion of Pontoon-2 and 9 are shown in Fig. 8 together with an RAO of the strong axis bending moment at the middle of the tower main span between Sec-0 and Sec-6. At larger wave periods, the peaks in these RAOs are closely linked to the first- and second mode horizontal motion illustrated in Fig. 7. For the shorter waves, the behaviour is more complex, as many of the vertical modes of the bridge are coupled to the horizontal response due to the curvature and the height of the bridge girder. Fig. 8(a) depicts the largest transverse pontoon motion, found at Pontoon-2 with RAO values up to 5 m/m around the first natural period of the structure and close to 1 m/m around the second natural period. As the pontoon number increase, the RAO peak at the first structural mode decreases, while the peak at the second mode – although it only varies slightly – becomes more significant, cf. Fig. 8(b). Due to space considerations, the YPOS response is only shown for the two outer pontoons, while the other pontoons follow the mentioned trend, caused by the changing dominance in the first and second horizontal modes depicted in Figs. 7(a) and 7(d). The corresponding strong axis bending moment in Fig. 8(c) shows the same overall behaviour as the transverse pontoon motion responses, as expected.

The torsional response is observed in the pontoon pitch motion and the bridge girder torsional moment, shown in Fig. 9, of which Figs. 9(a) and 9(c) reflect the largest RAO peaks for the pontoon pitch motion and bridge girder torsional moments, respectively. Similar to the transverse pontoon motions described previously, the pontoon pitch motion is dominated by the first natural period of the bridge, with the second structural mode becoming increasingly significant as the pontoon number increase. This is due to the fact that the peak around the second mode only has small variations while a consistent decrease in the peak around the first mode is observed, see Fig. 9(b). The influence from the 3rd, 4th and 5th modeshape is seen as the peaks around 8.5 s, 7.5 s and 6.5 s, respectively, most clearly seen in Fig. 9(b). The girder torsional moment RAOs, however, show a slightly different behaviour. Generally, these RAOs show the same behaviour as the pontoon pitch motion, although they seem to be excited more at lower wave periods where many of the more complex structural modes, cf. Fig. 5, are activated. The most dominating peaks observed in Figs. 9(c) and 9(d) correspond to the natural frequencies of the modes between the 9th and the 15th modeshape. The corresponding RAOs from the numerical model seem to capture the same general behaviour across the wave frequency range, although the amplitudes are somewhat lower for wave periods of 9 s and above.

The bridge vertical response is governed by multiple structural modes, including modes with dominating motion in the horizontal plane. Due to the complex geometry, the motions in the vertical and horizontal plane will always be coupled to some extend. In addition, the vertical bridge motion will tend to follow the wave for larger wave lengths, observed as the vertical motion RAOs going towards 1 m/m as the wave period increases. Selected RAOs related to the vertical bridge response are shown in Fig. 10 to facilitate a description of the general observations made from the tests. The pontoon motion RAOs shown in Fig. 10(a) are seen to go towards 1 m/m as previously discussed and show very clear peaks around 6.8 s and 10.0 s. The RAO calculated from the numerical model does not show the same increase in amplitude at these two wave frequencies, nor do they match any of the natural periods related to vertical modeshapes estimated from the numerical model. Possible reasons for this difference will be discussed in Section 4.1.5. In the pontoon vertical motion RAOs, there are also many other distinct peaks, particularly for waves with periods below 7.0 s, since many vertical modes are active in this frequency range. Unfortunately it is difficult to say anything specific regarding these peaks, as it is difficult to link them to any particular natural frequency due to their close proximity.

4.1.2. Wave response for waves propagating into the fjord at 220 degrees without current

The waves propagating at a 220 degree angle are close to perpendicular to the bridge longitudinal axis and roughly opposite to the waves propagating at 85 degrees, discussed earlier. Hence, the same first two structural modes are dominating the response characteristics throughout the bridge. The excitation of the horizontal motion along the bridge for wave periods close to these two natural periods, shown in Fig. 11, is seen to be even more pronounced than for waves with a 85 degree heading angle, as shown in Fig. 7.

An overview of the measured five DOF (excluding axial DOF) force RAOs along the bridge girder are shown in Fig. 12. Due to space consideration, only a selection of the locations listed in Table 2 are shown. Although several regular wave tests were also performed for this wave direction, the figure only shows the response from broad-banded irregular waves in order to illustrate the general behaviour more clearly. For instance, if the girder force responses are grouped according to their location along the bridge, there seems to be three distinct types of behaviour, related to: the cable-stayed tower; along the floating bridge section; and at END2. Focusing on the force RAOs related to the horizontal motion response first, the magnitude of the peak in MX close to the first structural mode match well with the shape

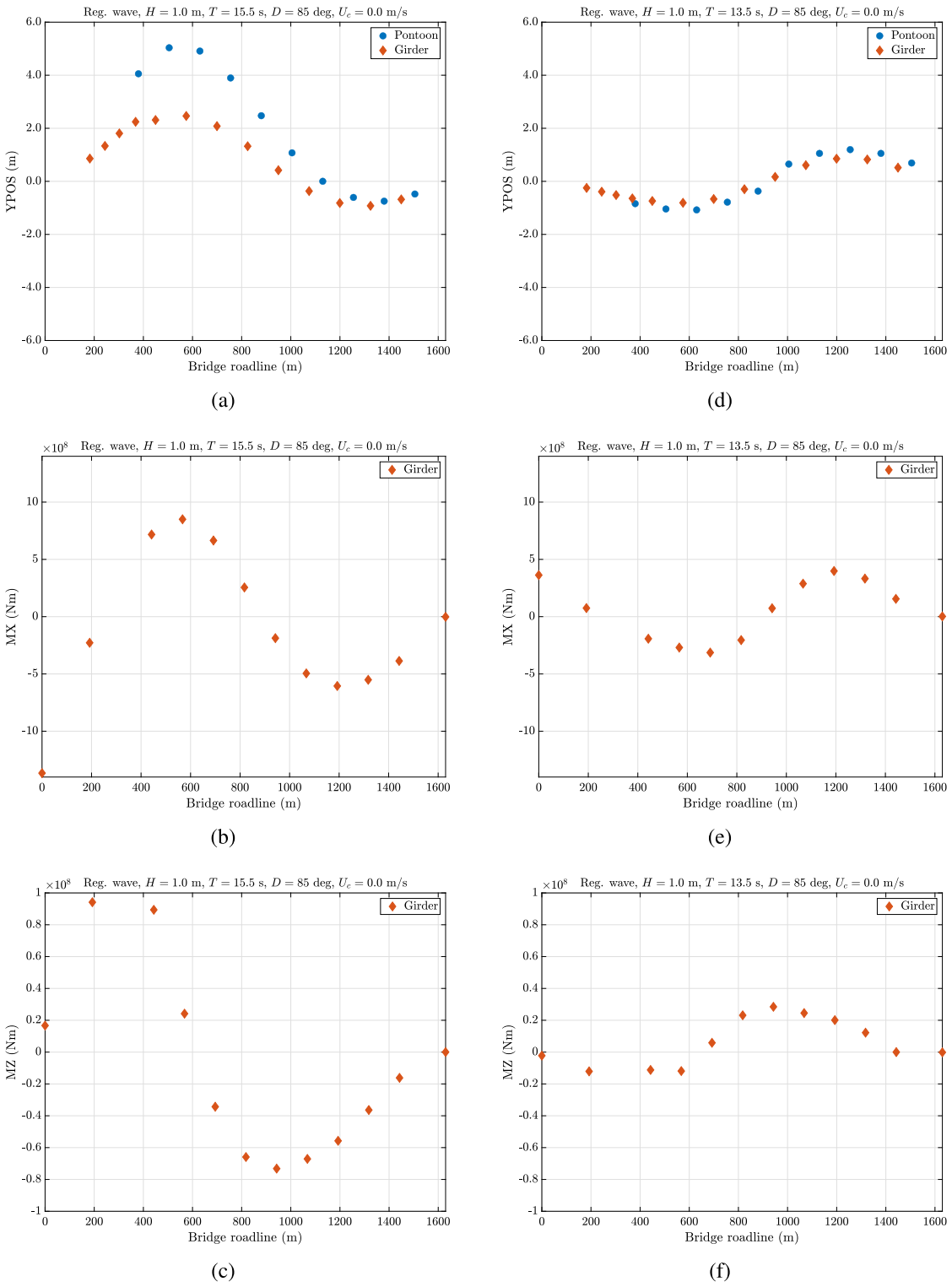

Fig. 7. Time instance of selected first harmonic responses along the bridge for two regular wave tests with $\theta = 85$ deg, $H = 1.0$ m and $U_c = 0.0$ m/s. Responses in (a)–(c) and (d)–(f) are transverse motion, strong axis bending moment and torsional moment along the bridge for a wave period close to the first and second natural period of the structure, respectively.

shown in Fig. 7(b). Although this shape is for waves propagating at 85 degrees, the same behaviour is found for 220 degrees. Following Euler–Bernoulli beam theory, bending moments are linked to the beam curvature. From the motion responses in Fig. 7(a), one can see how the dynamic bridge motion response curves the bridge in the horizontal plane. Starting at zero deflection at Sec-0, the bridge moves in the positive YPOS direction towards a maximum at Sec-7, followed by a decline towards zero-deflection around Sec-11. From there the bridge continues to move in the negative YPOS direction towards a negative maximum at Sec-13. From here the bridge moves back to a zero-deflection at Sec-16. The corresponding curvature is zero around Sec-2, Sec-10 and Sec-16, roughly corresponding to the measurement locations HB2, FB5 and END2. The largest absolute curvatures are found at Sec-0, between Sec-6 and Sec-7 and between Sec-12 and Sec-13, roughly corresponding to

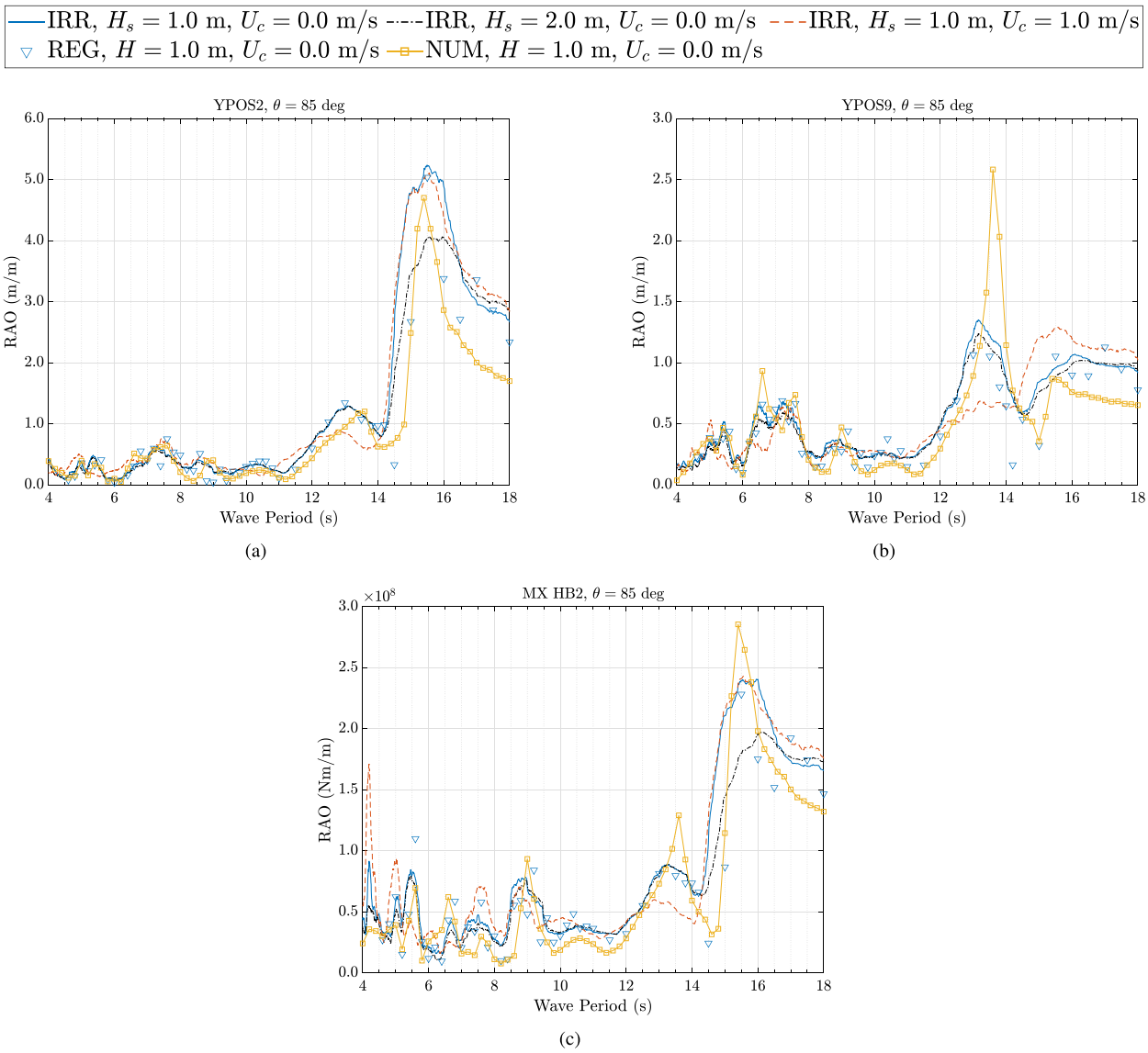

Fig. 8. RAOs illustrating the model horizontal response for waves propagating at θ = 85 degrees with and without collinear current. The IRR/REG/NUM notations used for the legend description refers to tests with irregular long-crested waves from a broad-banded wave spectrum, regular waves and numerically simulated regular wave response, respectively.

measurement locations END1, FB1 and FB7, respectively. At END2, the bridge girder is allowed to rotate freely, hence the strong axis bending moment is zero. The horizontal girder shear force FY is roughly the same at END1 and at HB2, due to relatively small cable tension force components aligned with the girder FY direction. Along the floating bridge section, the shear force is largest at FB5, corresponding to the zero-deflection point of the first horizontal mode. Inertia forces from the pontoons on either side are likely reasons for the largest shear force occurring at exactly this position. The torsional moment MZ along the bridge also show significant peaks around the first structural mode, as expected. This peak in the torsional moment around the first structural mode is most pronounced at HB2 and is related to the large YPOS and PITCH motion of the pontoons closest to the tower. The same peak in the torsional moment, related to the first structural mode, is significantly reduced at END1, which suggests that the torsion of the bridge girder to a large extent is absorbed by tension forces in the tower stay-cables. This is supported by clear peaks in the cable tension RAOs around 15.5 s, shown in Fig. 13 for the six cables closest to Pontoon-1, attached to the girder at Sec-3, 4 and 5. The RAOs for the other four cables are not shown as they are very similar to that of the cables connecting to the girder at Sec-3.

The girder force RAOs in Fig. 12 related to the vertical motion response, are the vertical shear force FX, the weak axis bending moment MY and the cable tension force. In the same way the cables restrict the torsional motion of the bridge girder between the tower and the first pontoon, they also restrict the vertical motion. Both the vertical shear force and the weak axis bending moment reflect this behaviour in their significantly lower RAO amplitudes at END1 and HB2. Along the floating bridge section, the same force responses show significantly larger amplitudes. Generally, this is due to the many active modes of the bridge girder at this frequency range, contributing to the vertical motion.

The bridge girder axial force at the two ends of the bridge is shown in Fig. 14 for both regular waves and broad-banded irregular waves with and without current. From the RAOs it is clearly seen that the axial forces are dominated by the first two structural modes, while smaller peaks are observed in the RAOs for wave periods of 8.5 s and 7.5 s close to the 3rd and 4th structural modes, respectively.

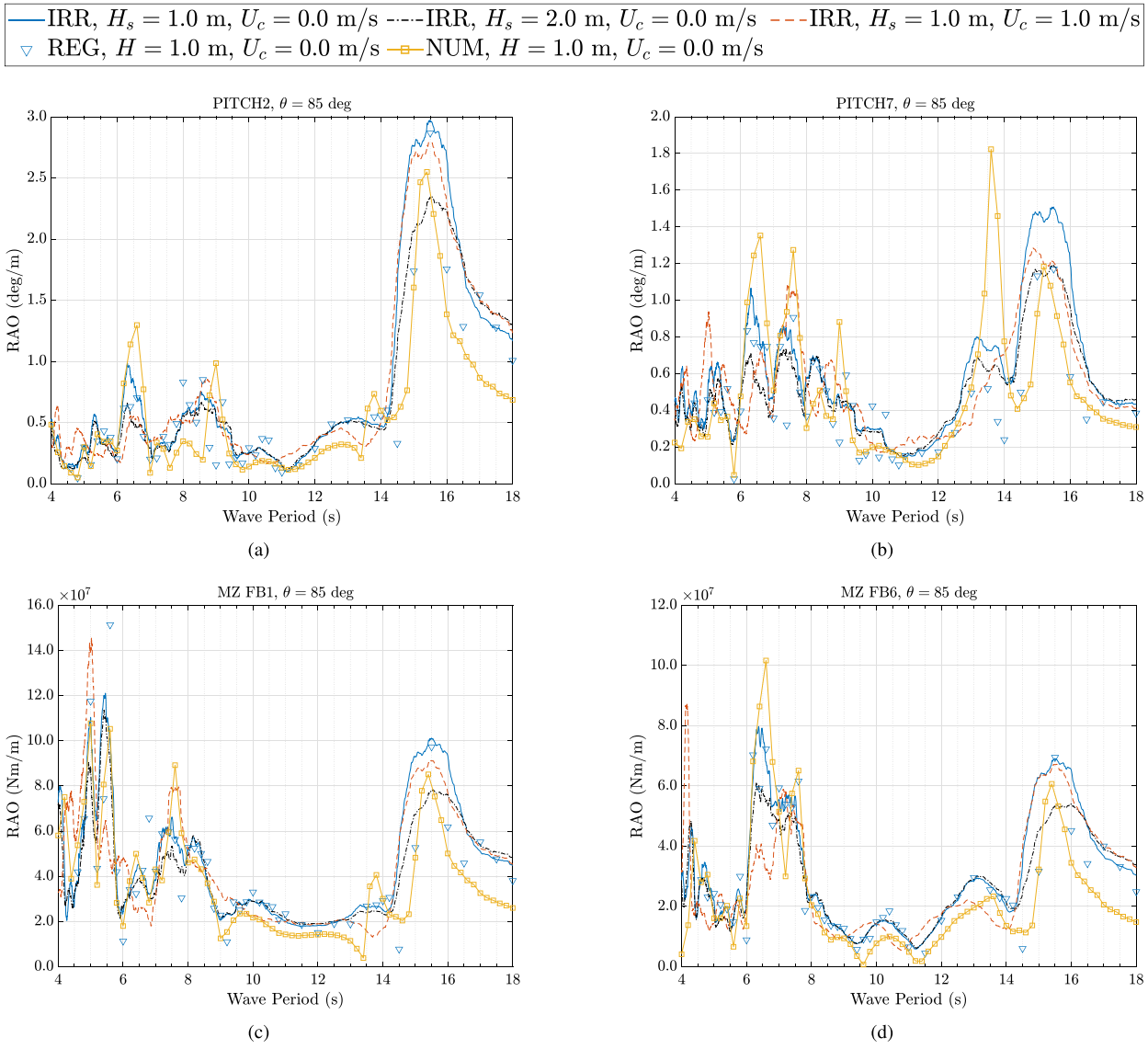

Fig. 9. RAOs illustrating the model torsional response for waves propagating at $\theta = 85$ degrees with and without collinear current. The IRR/REG/NUM notations used for the legend description refers to tests with irregular long-crested waves from a broad-banded wave spectrum, regular waves and numerically simulated regular wave response, respectively.

4.1.3. Asymmetric cable tension behaviour

An interesting behaviour is observed in the cable tension RAOs for waves travelling at 220 degrees, seen in Fig. 13. The tension in the cables on the two sides of the bridge do not show the same response characteristics, which is most clearly illustrated by the difference in the RAO values for the axial force in CB EAST 18 and CB WEST 18 — particularly for wave periods close to 14.0 s. From the numerically calculated modeshapes, it is found that the first modes, although clearly dominated by horizontal- and torsional motion, also consisted of vertical motion of the bridge girder at the cable-stayed tower section. Particularly the combination of vertical- and torsional motion of the bridge girder resulted in significant vertical motion at the attachment point for CB EAST 18, while at the same time the location for CB EAST 18 almost did not move vertically. This effect is thought to be the main cause of the dip in tension for CB WEST 18 close to 14 s when compared to CB EAST 18.

4.1.4. Notable non-linear response characteristics for waves without current

Non-linear wave response is observed for various measurements along the bridge model for wave propagating at 85 and 220 degrees. For transverse motion responses (YPOS and PITCH) and the corresponding girder force responses (FY, MX and MZ), a clear reduction is observed in the RAO values, particularly around the peak related to the first structural mode. The reduction is also present at the second structural mode and for wave periods $T \leq 8.0$ s, although less significant. As the second and third natural periods of the experimental model are 13.5 s and 8.5 s, respectively, it is clear that no structural modes are activated by waves with periods between these two natural periods of the structure, resulting in fewer non-linear wave response effects. Finally, the bridge girder axial forces at the two ends related to the horizontal motion show a significant reduction in the peak at the first structural mode for both wave directions. For vertical responses the non-linear effects are relatively small but generally seem to slightly increase the response for longer waves and slightly reduce the response for shorter waves. The tension response in the tower stay-cables is influenced by both vertical and torsional motion and show a significant reduction in the peak related to the first structural mode. Some reduction is also observed for wave periods below 8.0 s.

4.1.5. Possible effects from hydrodynamic interaction between the pontoons

Investigations into the hydrodynamic interaction between the pontoons is a topic outside the scope of the present paper but due to

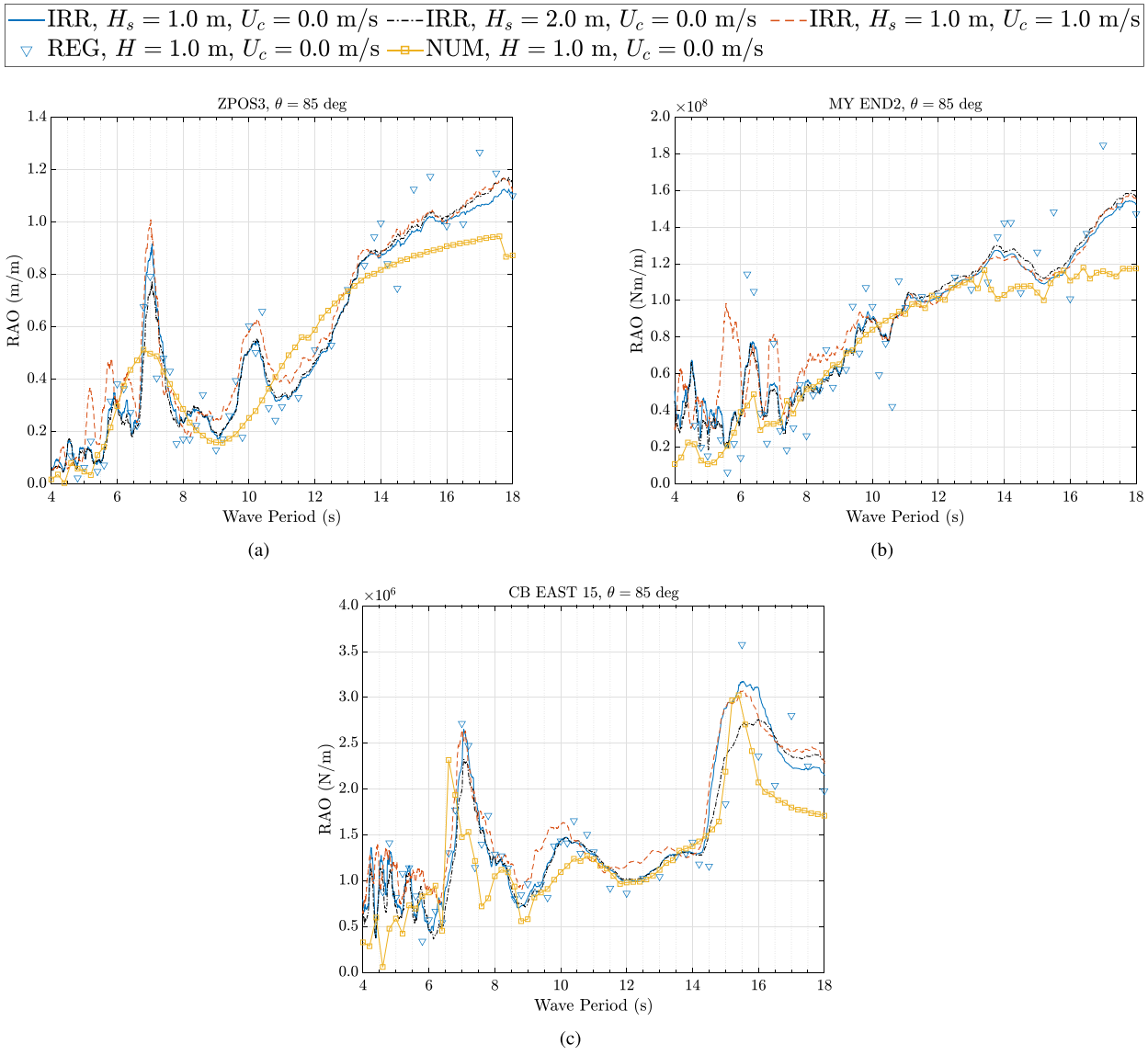

Fig. 10. RAOs illustrating the model vertical response for waves propagating at $\theta = 85$ degrees with and without collinear current. The IRR/REG/NUM notations used for the legend description refers to tests with irregular long-crested waves from a broad-banded wave spectrum, regular waves and numerically simulated regular wave response, respectively.

the relatively short distance between the pontoons and their structural dimensions, it is expected that hydrodynamic interaction effects are influencing some of the measured responses. From previous numerical studies (Xiang et al., 2018; Fenerci et al., 2022) on hydrodynamic interaction related to curved floating bridges with discrete pontoons, the responses related to horizontal motion of the bridge are found to not be affected by the hydrodynamic interaction between the pontoons. Instead, hydrodynamic interaction influences the responses related to the bridge vertical motion (Xiang et al., 2018; Fenerci et al., 2022) as well as the girder axial force (Fenerci et al., 2022). The findings reported in Fenerci et al. (2022) will be used as reference in the present discussion, as the bridge is conceptually similar to the one described here. However, it is worth keeping in mind that the centre-line spacing between the pontoons in Fenerci et al. (2022) is 100 m and their length is 58 m. Most of these pontoons have a width of 10 m, except for a few pontoons with larger widths of 12 m, 14 m and 16 m.

By comparing the measured RAOs from waves only tests to the corresponding RAO results obtained from the numerical model and the natural periods of the structure, it is possible to get an idea of whether or not hydrodynamic interaction is present in the model test. In situations where the numerically obtained RAOs are relatively smooth and the measured RAOs show the same trend but with notably more frequent changes in the amplitude it is possible that this is due to hydrodynamic interaction effects. Keeping in mind the uncertainties related to this crude approach, some general comments can be made:

- Starting with the RAOs related to the horizontal bridge motion, depicted in Fig. 8, it is clear that the same general behaviour is captured in the numerical model as in the experiments, which is aligned with the findings from the literature.
- The measured RAOs related to the torsional bridge motion, depicted in Fig. 9, show a large number of local peaks in the range below wave periods of 10 s. This behaviour is also captured in the numerical model, which makes it unlikely that any hydrodynamic interaction is of any importance to these responses.
- Some significant differences are observed between the numerical and measured RAOs related to vertical motion of the bridge as seen in Fig. 10, which suggest a strong influence from hydrodynamic interaction between the pontoons. This is again supported by the findings in the literature.

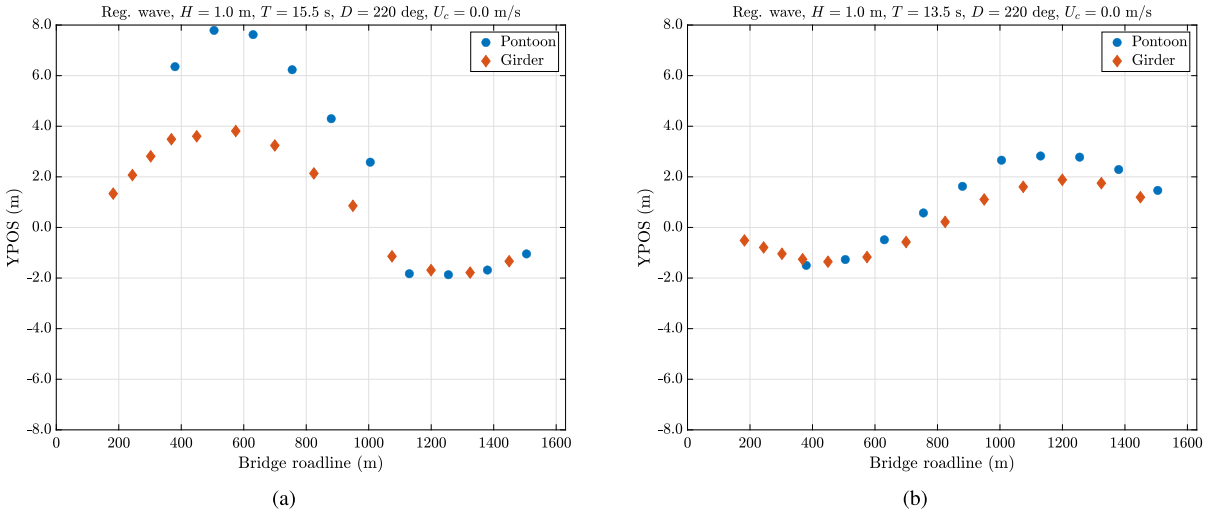

Fig. 11. Time instance of selected first harmonic horizontal responses along the bridge for regular waves propagating at $\theta = 220$ deg with $H = 1.0$ m and $U_c = 0.0$ m/s. Responses in (a) and (b) are transverse motion perpendicular to the bridge roadline for regular waves with period of 15.5 s, 13.5 s, respectively. The time instance is when the largest pontoon motion along the bridge occurs.

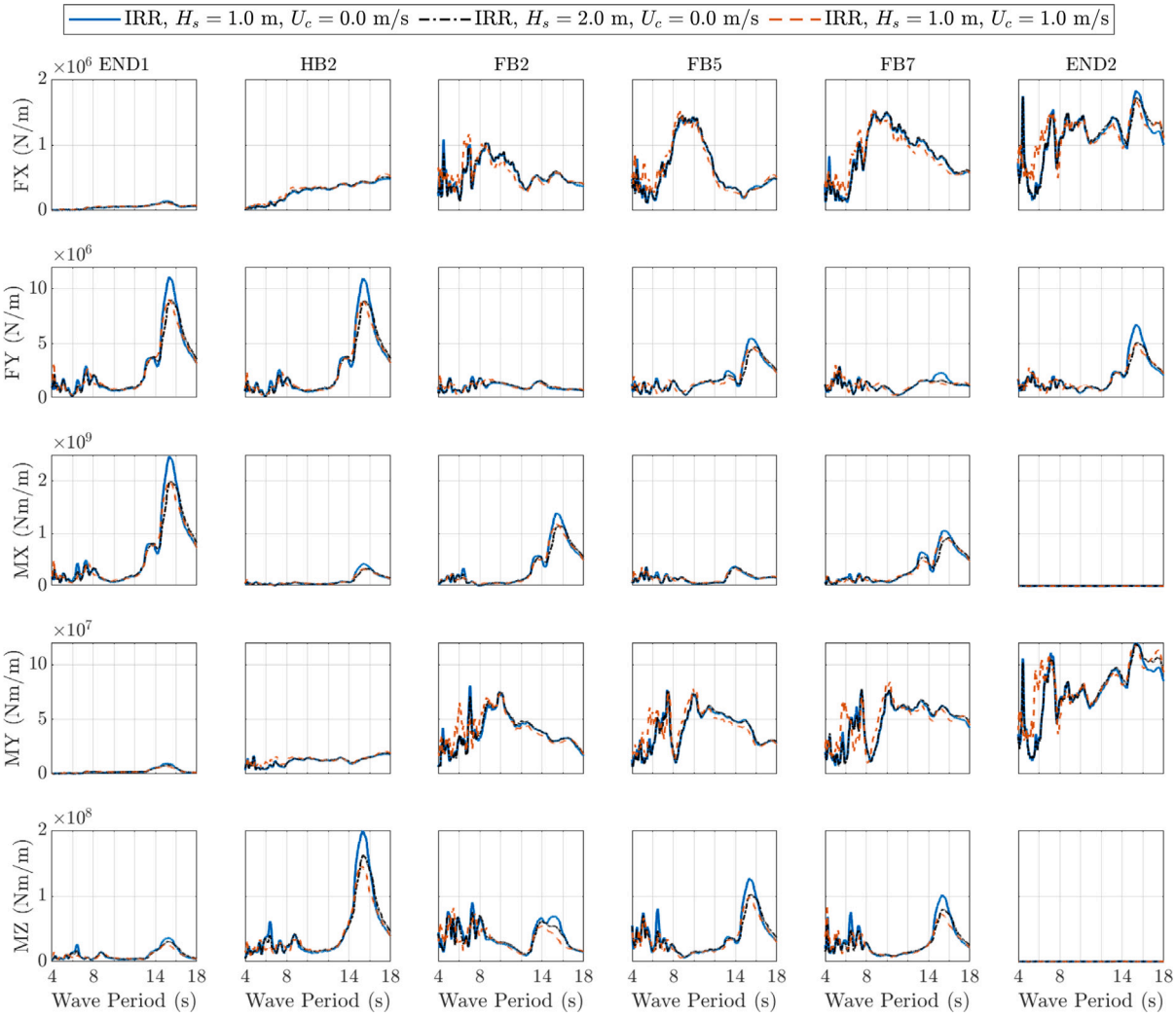

Fig. 12. Bridge girder force RAOs at selected locations along the bridge based for irregular, broad-banded waves propagating at a 220 degree angle with and without current. Each row is for a specific force response and each column is for a specific location along the bridge girder. See Table 2 for the location names. The IRR notations used for the legend description refers to tests with irregular long-crested waves from a broad-banded wave spectrum.

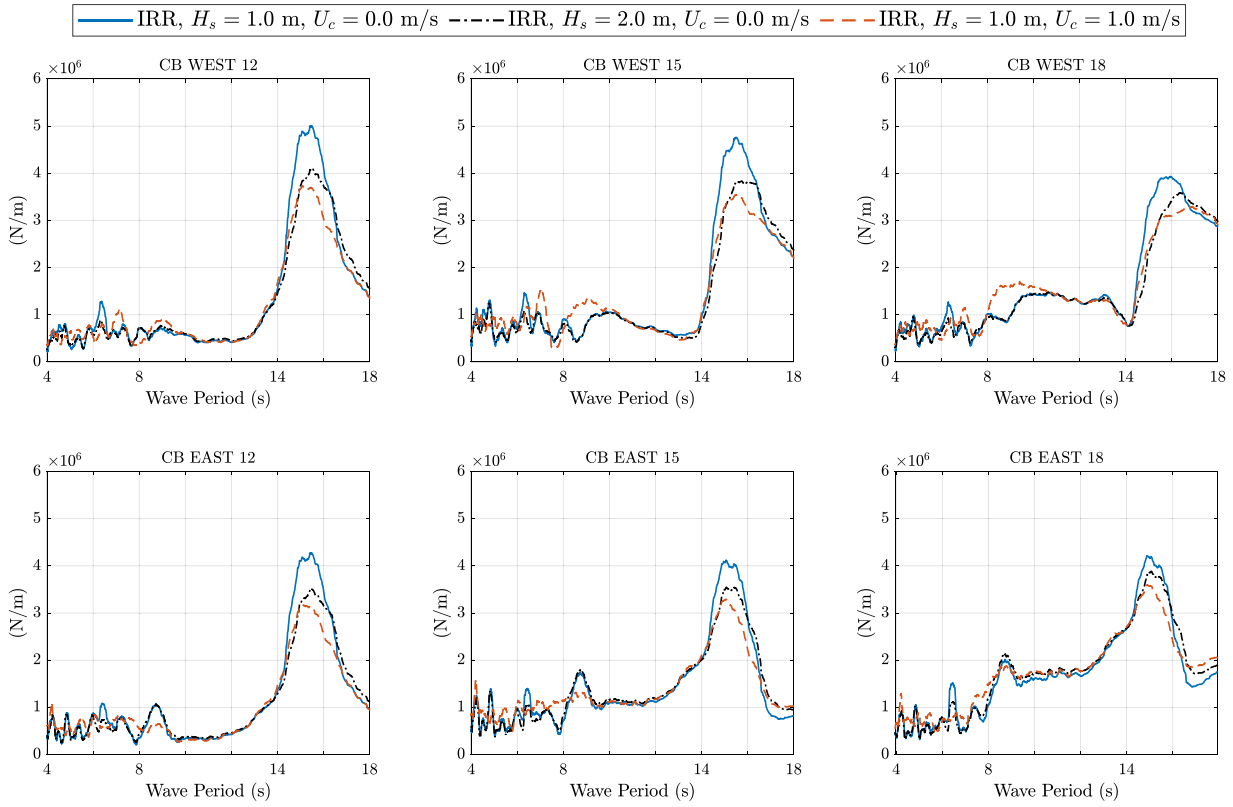

Fig. 13. Cable tension RAOs at selected locations along the cable-stayed bridge section for irregular, broad-banded waves propagating at a 220 degree angle with and without current. Each row is for a specific side of the bridge and each column is for a specific cable set along the bridge girder. The set numbers 12, 15 and 18 relate to the cable sets attached to the bridge girder at Sec-3, 4 and 5, respectively. See Fig. 1 for location names. The IRR notations used for the legend description refers to tests with irregular long-crested waves from a broad-banded wave spectrum.

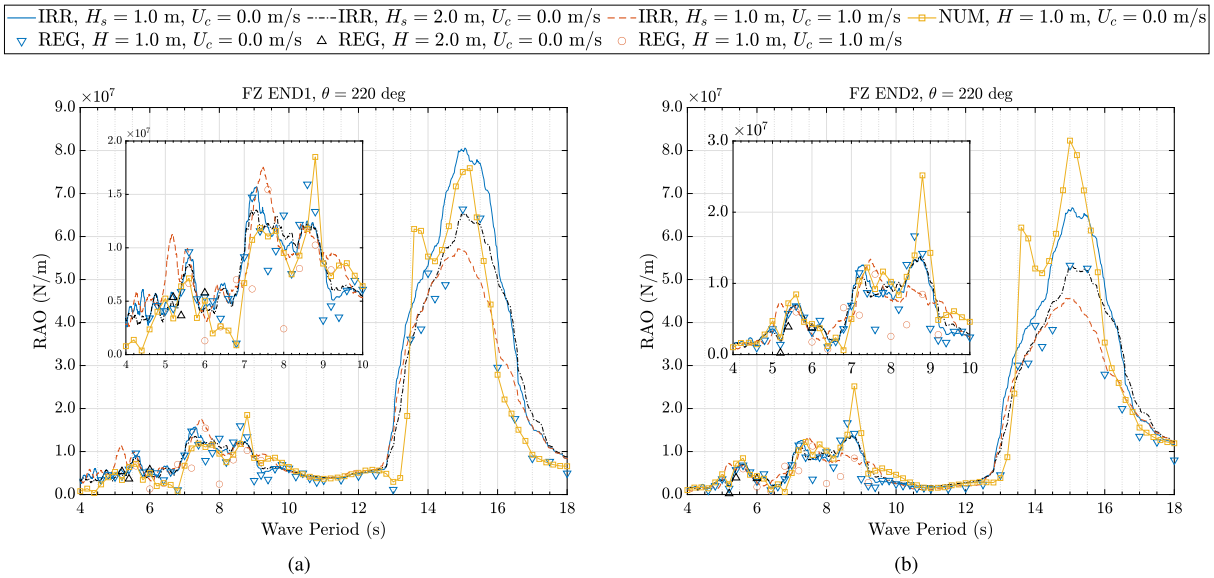

Fig. 14. Bridge girder axial force RAO at END1 and END2 for waves propagating at a 220 degree angle with and without current. The IRR/REG/NUM notations used for the legend description refers to tests with irregular long-crested waves from a broad-banded wave spectrum, regular waves and numerically simulated regular wave response, respectively.

- The axial force RAOs depicted in Fig. 14 show the same behaviour in the numerical and empirical responses, which goes against the findings from Fenerci et al. (2022). However, these observations are based on a general, visual comparison of RAOs, whereas the findings in Fenerci et al. (2022) were based on root-mean-square results found by integrating the response spectra.

4.1.6. Observable effects of current travelling with the waves

For each RAO figure previously discussed, the values are shown for the structure subjected to waves only and when subjected to waves and a current of 1.0 m/s travelling with the waves. Comparing the RAOs related to the horizontal bridge response in Fig. 8 for waves propagating at a 85 degree angle with and without current, the YPOS

motion for wave periods close to the first and second structural mode is seen to be affected differently, depending on the pontoon number. For the pontoons closest to the cable-stayed tower, as exemplified in Fig. 8(a), the transverse pontoon motion is reduced by the current for wave periods close to the second structural mode, while the peak in the RAOs related to the first mode is unaffected. As the pontoon number increases, the peak around the first natural period of the structure continues to reduce in amplitude as an effect from the current. This effect continues until Pontoon-6 or 7, after which the same peak starts to grow as the pontoon number continues to increase. This trend continues until the RAOs for the pontoon transverse motion look like the one depicted in Fig. 8(b). For wave periods close to the first and second structural mode, the pontoon PITCH motion, cf. Fig. 9, is also diminished by the presence of the current. The pontoon YPOS and PITCH motion is linked to the bridge girder strong axis bending moment MX responses, depicted in Fig. 8(c). Generally, the peak in the MX RAOs around 13.5 s is reduced by the current, while the peak around 15.5 s is slightly increased by the current (effect not seen in Fig. 8(c)). The RAOs related to torsional responses show an interesting behaviour around the shorter waves where many of the complex structural modes, dominated by vertical motion, are active. The fact that many modes are active around the same wave periods makes it difficult to interpret the results, as one mode might be more excited when no current is present, while another is more excited by waves with collinear current. The result is various RAO peaks moving in opposite directions making it difficult to draw out any clear conclusion and the effect of the current seem to simultaneously amplify and reduce the responses in the frequency range related to wind wave load excitation. The bridge girder force RAOs for waves and current propagating at 220 degrees from North, cf. Fig. 12, show a similar behaviour along the bridge, although the effect of the current does not seem to increase the peaks related to the first structural mode. Instead, the peak is significantly reduced for responses such as FY, MX and MZ.

When comparing the RAOs related to the vertical responses along the bridge for waves propagating at an 85 degree angle with and without collinear current, the reader is referred to Fig. 10 with selected responses along the bridge. A general observation along the bridge is that the vertical motion response, for most wave periods, is slightly amplified by the current — with most of the amplification at wave periods at 10 s and below. As an example, the vertical pontoon motion and the weak axis bending moment depicted in Figs. 10(a) and 10(b), respectively, show a significant increase in amplitude for waves with periods close to 5.5 s. Instead, the cable tension, girder vertical shear force and weak axis bending moment RAOs corresponding to the vertical motion, generally seem to be reduced slightly for wave periods above 10 s and slightly amplified for lower wave periods. For waves and current propagating in the opposite direction into the fjord, the same general behaviour is observed. Here the reader is referred to Fig. 12 for the force response at selected locations along the bridge and to Fig. 13 for the cable tension RAOs. For wave periods roughly below 10 s there is a general increase in the cable tension and bridge girder FX and MY RAOs when current is present, except at a few select wave periods. Particularly around wave periods close to 5.5 s, there is a significant increase in the girder FX and MY responses when current is present.

4.2. Effects of current on long-crested wind and swell wave responses

4.2.1. Case with 100-year wind waves

Tables 5 and 6 list the normalized standard deviations of selected motion and force responses, respectively, for the long-crested wave condition governed by the wave spectrum parameters corresponding to the 100-year wind wave condition. The response standard deviations are normalized to the standard deviation of the measured wave elevation and the waves are propagating at a 220 degree angle with and without collinear current.

From the standard deviations listed in Table 5, the pontoon motion responses are all seen to be significantly affected by the current — an effect which increases with the current velocity. The pontoon responses related to horizontal motion of the bridge, i.e. YPOS and PITCH, are on average reduced by 1% and 11%, respectively when subjected to a 1-year current velocity compared to the same wave scenario without any current. The same averaged reductions increase to 4% and 13% when subjected to a 10-year current velocity. The transverse motion of the individual pontoons show that most of the reduction in YPOS stems from the pontoons on either side of the bridge centre position, while a slight increase in YPOS is observed at the middle pontoons. Disregarding any possible effects from hydrodynamic interaction between the pontoons, as per the discussion in Section 4.1.5, a plausible reason is that most of the active structural modes have a zero-deflection point close to the middle of the bridge length, cf. Fig. 5, which diminishes any effect from the current in this area. In the case of the pontoon responses related to the vertical motion of the bridge, i.e. XPOS and ZPOS, the current has an opposite, amplifying effect. These two response types are on average increased by 35%–54%, depending on the current velocity. This effect is more or less consistent for all the individual pontoons along the bridge.

The effect of the current on the standard deviations for the bridge girder and stay-cable force responses is seen in the response ratios in Table 6. It is clear that the horizontal shear force FY of the bridge girder is increased when current is present, although the effect is opposite at locations close to the tower. This effect does not seem to increase with the current velocity. A possible explanation for this could be that the increase in the shear force from the increased uniform current is cancelled out by a reduction in the shear force from pontoon motion inertia due to less transverse pontoon motions. The strong axis bending moment MX show, on average, little influence from the current. However, when looking at the individual measurement locations, it is clear that for some locations the responses are increased by the current, while other are reduced.

The torsional girder moments MZ show on average no significant changes when current is present in the tests. However, this average value hides the fact that the response is generally slightly increased, except for positions END1 and HB2, which both show significant reductions. To understand why this is, the reader is referred to the corresponding response spectra, cf. Fig. 15. For both locations the response spectra show three clear peaks at wave frequencies close to the wave spectrum peak frequency (0.18 Hz), for the case without waves. When current is present, the two peaks not coinciding with the wave spectrum peak frequency are significantly reduced, resulting in an overall decrease of the area below the spectrum curve and hence the response standard deviations.

The force and moment responses related to vertical motion of the bridge show the same increase in standard deviations when current is present and when said current velocity is increased. This is clearly seen in the FX, MY and CB standard deviations listed in Table 6. This effect is both significant and covers all the listed, individual measurement locations. In the case of the vertical shear force and the weak axis bending moment, this effect could be explained by the increasing RAO values around the wave spectrum peak period when current is present, cf. Figs. 10(b) and 12. The stay-cable tension behaviour is more complex, although a similar but less significant increase in the RAO values is observed in Figs. 10(c) and 13 when current is present.

The bridge girder axial force FZ is, contrary to the other measured force responses, also influenced by wave frequencies outside the proximity of the wave spectrum peak frequency, cf. Fig. 15, which excite the first and second structural modes. When current is present these two modes are significantly reduced, which cancels out the amplifications observed at wave frequencies close to the wave peak frequency. This is the reason for the only small increases in the standard deviation values listed in Table 6.

The above mentioned findings corroborate numerical studies found in the literature (Xiang and Løken, 2019; Viuff et al., 2020; Dai et al.,

Table 5
Normalized standard deviation of pontoon motion responses subjected to a 100-year wind wave condition with and without 1-year or 10-year current. The column values referring to responses without current are the ensemble average standard deviations from 10 statistically independent wave tests with different wave seed numbers. Both waves and current are propagating at an angle of 220° from North.

Parameter	Unit	Value			Ratio		Parameter	Unit	Value			Ratio	
U_c	(m/s)	0.00	1.00	1.44			U_c	(m/s)	0.00	1.00	1.44		
H_s (target)	(m)	2.10	2.10	2.10	$\frac{U_c=1.00\ m/s}{U_c=0.00\ m/s}$	$\frac{U_c=1.44\ m/s}{U_c=0.00\ m/s}$	H_s (target)	(m)	2.10	2.10	2.10	$\frac{U_c=1.00\ m/s}{U_c=0.00\ m/s}$	$\frac{U_c=1.44\ m/s}{U_c=0.00\ m/s}$
H_s (meas.)	(m)	2.03	1.96	1.93			H_s (meas.)	(m)	2.03	1.96	1.93		
T_p	(s)	5.50	5.50	5.50			T_p	(s)	5.50	5.50	5.50		
XPOS1	(m)	0.131	0.179	0.186	1.37	1.42	YPOS1	(m)	0.365	0.360	0.334	0.99	0.92
XPOS2	(m)	0.111	0.143	0.151	1.28	1.35	YPOS2	(m)	0.295	0.288	0.293	0.98	0.99
XPOS3	(m)	0.094	0.133	0.154	1.41	1.64	YPOS3	(m)	0.460	0.412	0.377	0.90	0.82
XPOS4	(m)	0.087	0.128	0.117	1.46	1.34	YPOS4	(m)	0.304	0.310	0.294	1.02	0.97
XPOS5	(m)	0.084	0.098	0.115	1.16	1.36	YPOS5	(m)	0.263	0.260	0.249	0.99	0.95
XPOS6	(m)	0.071	0.107	0.112	1.51	1.59	YPOS6	(m)	0.307	0.326	0.310	1.06	1.01
XPOS7	(m)	0.064	0.082	0.110	1.28	1.71	YPOS7	(m)	0.215	0.235	0.231	1.09	1.08
XPOS8	(m)	0.053	0.087	0.091	1.63	1.71	YPOS8	(m)	0.169	0.147	0.153	0.87	0.91
XPOS9	(m)	0.045	0.067	0.095	1.47	2.10	YPOS9	(m)	0.234	0.232	0.233	0.99	1.00
XPOS10	(m)	0.043	0.047	0.051	1.10	1.18	YPOS10	(m)	0.211	0.208	0.212	0.99	1.01
Average					1.37	1.54	Average					0.99	0.96
ZPOS1	(m)	0.114	0.140	0.164	1.23	1.44	PITCH1	(deg)	0.495	0.460	0.421	0.93	0.85
ZPOS2	(m)	0.124	0.152	0.161	1.23	1.30	PITCH2	(deg)	0.375	0.330	0.331	0.88	0.88
ZPOS3	(m)	0.140	0.155	0.160	1.11	1.14	PITCH3	(deg)	0.541	0.454	0.424	0.84	0.78
ZPOS4	(m)	0.131	0.157	0.189	1.20	1.45	PITCH4	(deg)	0.402	0.413	0.399	1.03	0.99
ZPOS5	(m)	0.141	0.208	0.187	1.48	1.33	PITCH5	(deg)	0.376	0.372	0.376	0.99	1.00
ZPOS6	(m)	0.170	0.204	0.221	1.20	1.30	PITCH6	(deg)	0.497	0.489	0.477	0.98	0.96
ZPOS7	(m)	0.155	0.270	0.280	1.74	1.81	PITCH7	(deg)	0.516	0.486	0.467	0.94	0.90
ZPOS8	(m)	0.169	0.226	0.268	1.34	1.59	PITCH8	(deg)	0.467	0.380	0.360	0.81	0.77
ZPOS9	(m)	0.217	0.327	0.340	1.50	1.56	PITCH9	(deg)	0.485	0.357	0.352	0.74	0.73
ZPOS10	(m)	0.183	0.268	0.346	1.46	1.89	PITCH10	(deg)	0.554	0.428	0.439	0.77	0.79
Average					1.35	1.48	Average					0.89	0.87

NB: Values are normalized w.r.t. the standard deviation of the measured wave elevation, i.e. one fourth of the listed H_s (meas.) values.

Table 6
Normalized standard deviation of selected girder and stay-cable force responses subjected to a 100-year wind wave condition with and without 1-year or 10-year current. The column values referring to responses without current are the ensemble average standard deviations from 10 statistically independent wave tests with different wave seed numbers. The cable tension forces are given as the average value for each set. Both waves and current are propagating at an angle of 220° from North.

Parameter	Unit	Value			Ratio		Parameter	Unit	Value			Ratio	
U_c	(m/s)	0.00	1.00	1.44			U_c	(m/s)	0.00	1.00	1.44		
H_s (target)	(m)	2.10	2.10	2.10	$\frac{U_c=1.00\ m/s}{U_c=0.00\ m/s}$	$\frac{U_c=1.44\ m/s}{U_c=0.00\ m/s}$	H_s (target)	(m)	2.10	2.10	2.10	$\frac{U_c=1.00\ m/s}{U_c=0.00\ m/s}$	$\frac{U_c=1.44\ m/s}{U_c=0.00\ m/s}$
H_s (meas.)	(m)	2.03	1.96	1.93			H_s (meas.)	(m)	2.03	1.96	1.93		
T_p	(s)	5.50	5.50	5.50			T_p	(s)	5.50	5.50	5.50		
FX END1	(N)	2.41E+04	4.70E+04	5.80E+04	1.95	2.40	MX END1	(Nm)	1.55E+08	1.49E+08	1.54E+08	0.96	0.99
FX HB2	(N)	7.41E+04	1.21E+05	1.47E+05	1.64	1.99	MX HB2	(Nm)	4.55E+07	5.00E+07	4.94E+07	1.10	1.09
FX FB2	(N)	4.03E+05	5.33E+05	5.71E+05	1.32	1.42	MX FB2	(Nm)	1.36E+08	1.31E+08	1.18E+08	0.97	0.87
FX FB5	(N)	3.59E+05	4.73E+05	5.04E+05	1.32	1.40	MX FB5	(Nm)	1.71E+08	1.80E+08	1.65E+08	1.05	0.97
FX FB7	(N)	3.58E+05	4.63E+05	5.25E+05	1.29	1.47	MX FB7	(Nm)	1.04E+08	9.54E+07	9.70E+07	0.91	0.93
FX END2	(N)	5.95E+05	7.10E+05	9.80E+05	1.19	1.65	MX FB9	(Nm)	1.94E+08	2.26E+08	2.21E+08	1.17	1.14
Average					1.45	1.72	Average					1.03	1.00
FY END1	(N)	9.81E+05	1.03E+06	1.05E+06	1.05	1.07	MY END1	(Nm)	7.43E+05	1.29E+06	1.49E+06	1.73	2.00
FY HB2	(N)	7.76E+05	7.57E+05	7.64E+05	0.98	0.98	MY HB2	(Nm)	6.90E+06	8.73E+06	1.01E+07	1.26	1.47
FY FB2	(N)	9.06E+05	1.01E+06	9.69E+05	1.11	1.07	MY FB2	(Nm)	2.31E+07	3.05E+07	3.49E+07	1.32	1.51
FY FB5	(N)	8.92E+05	1.08E+06	1.05E+06	1.21	1.18	MY FB5	(Nm)	2.33E+07	3.08E+07	3.49E+07	1.32	1.50
FY FB7	(N)	1.45E+06	1.66E+06	1.62E+06	1.15	1.12	MY FB7	(Nm)	2.18E+07	3.35E+07	4.33E+07	1.54	1.99
FY END2	(N)	1.35E+06	1.62E+06	1.62E+06	1.20	1.20	MY END2	(Nm)	4.06E+07	5.32E+07	7.28E+07	1.31	1.79
Average					1.12	1.10	Average					1.41	1.71
FZ END1	(N)	5.49E+06	6.27E+06	6.03E+06	1.14	1.10	MZ END1	(Nm)	7.65E+06	6.88E+06	6.35E+06	0.90	0.83
FZ END2	(N)	4.16E+06	4.13E+06	4.08E+06	0.99	0.98	MZ HB2	(Nm)	2.04E+07	1.90E+07	1.73E+07	0.93	0.85
Average					1.07	1.04	MZ FB2	(Nm)	4.44E+07	4.81E+07	4.30E+07	1.08	0.97
CB 12	(N)	5.18E+05	5.80E+05	6.14E+05	1.12	1.19	MZ FB5	(Nm)	3.74E+07	3.95E+07	3.80E+07	1.05	1.02
CB 15	(N)	6.97E+05	7.88E+05	8.70E+05	1.13	1.25	MZ FB7	(Nm)	2.57E+07	2.97E+07	2.93E+07	1.16	1.14
CB 18	(N)	5.99E+05	6.78E+05	7.49E+05	1.13	1.25	MZ FB9	(Nm)	1.92E+07	2.10E+07	2.15E+07	1.09	1.12
Average					1.13	1.23	Average					1.03	0.99

NB: Values are normalized w.r.t. the standard deviation of the measured wave elevation, i.e. one fourth of the listed H_s (meas.) values.

2022) stating that properly accounting for wave–current-interaction effects is important. These studies have validated their numerical models towards previously performed model tests (Aarsnes et al., 1990b) of a generic, curved floating bridge with discrete pontoons. Among other investigations, they investigated the effect of collinear current on the wave response. The model tests generally showed an increase in both vertical and horizontal responses when current travelled with the waves. Xiang and Løken (2019) and Viuff et al. (2020) modelled the as-build properties in OrcaFlex (Orcina, 2018) and SIMA (SINTEF Ocean, 2022), respectively, while accounting for wave–current-interaction effects on the first order wave forces only. Dai et al. (2022) recently performed a numerical study in SIMA on the effect on the

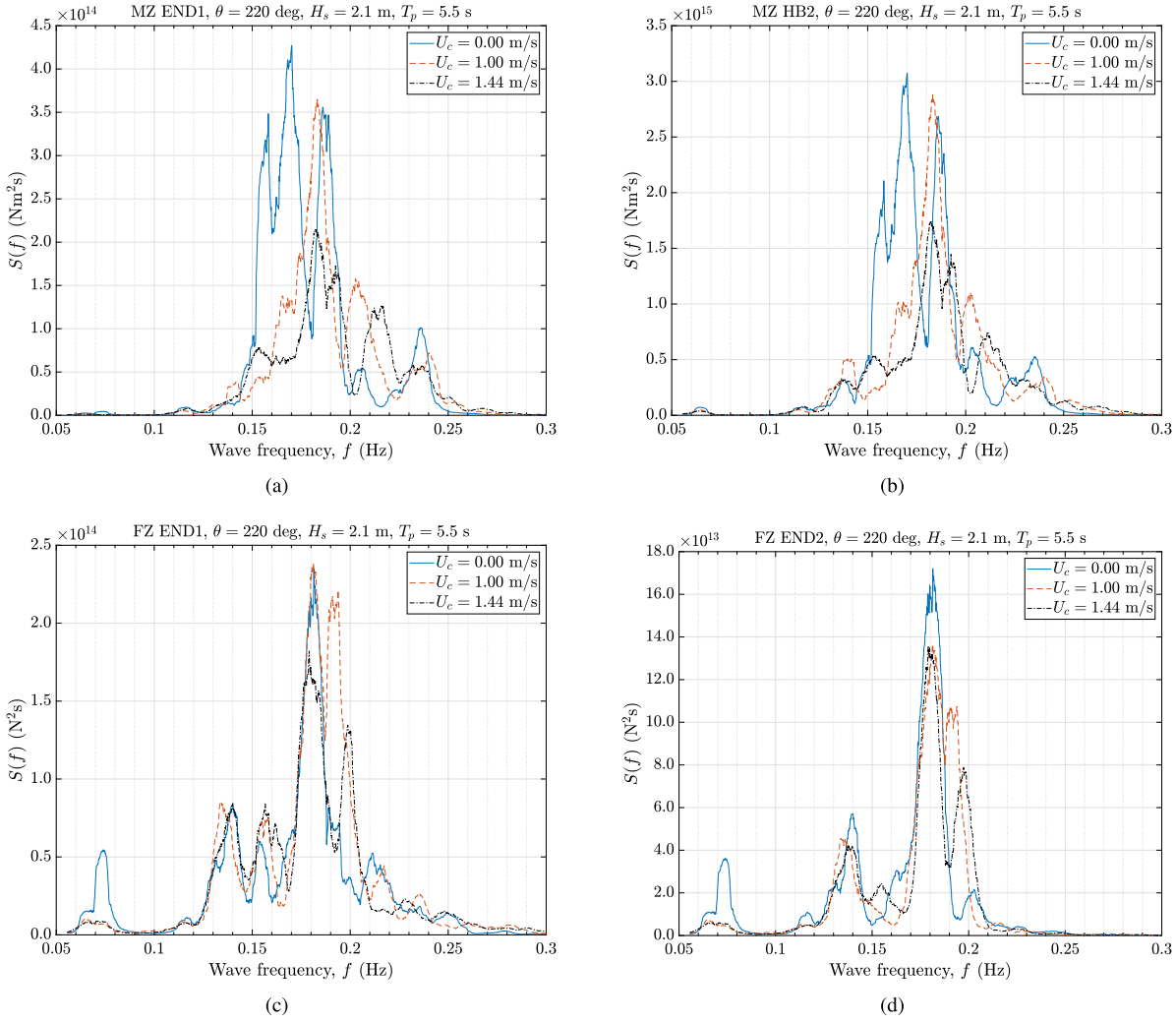

Fig. 15. Girder axial force and torsional moment response spectra when subjected to 100-year wind waves with and without 1-year or 10-year current velocities. (a) Girder torsional moment at END1. (b) Girder torsional moment at HB2. (c) Girder axial force at END1. (d) Girder axial force at END2.

predicted structural response when using various methods to account for current travelling with and against propagating waves perpendicular to a straight, side-anchored floating bridge with discrete pontoons. They found that it is important to accounting for the wave–current-interaction effect on both the first order wave force transfer functions as well as the frequency-dependent added mass and potential damping properties.

4.2.2. Case with 10000-year swell waves

Tables 7 and 8 list the normalized standard deviations of selected motion and force responses, respectively, for the long-crested wave condition governed by the wave spectrum parameters corresponding to the 10000-year swell wave condition. The response standard deviations are normalized to the standard deviation of the measured wave elevation and the waves are propagating at a 220 degree angle with and without collinear current.

From Table 7, the effect of current on the pontoon motion response is observed to have a different effect on the swell wave condition than on the previously discussed wind wave conditions. The pontoon YPOS and PITCH motion related to the horizontal response of the bridge is on average reduced by 18% and 21% for YPOS and PITCH pontoon motions, respectively, when subjected to a 1-year current. This is significantly more than for the wind wave condition. Contrarily, the pontoon XPOS motions are on average reduced by 7%, which is opposite to the behaviour during the wind wave condition. Similarly, the ZPOS motion shows on average only a 2% increase, which is significantly less than for the wind wave condition. Based on the standard deviations in Table 8, the current is observed to have a diminishing effect on all of the dynamic force and moment responses along the bridge. This drastic change in the structural behaviour is linked to the different distribution of the wave energy in the swell wave spectrum. With a wave peak period of 13.8 s close to the first and second structural mode of the model, the other modes (T_n < 8.5 s) are less significant for the response of the bridge. Hence, the response from the swell wave condition can be traced back to the lower amplitude values in the RAOs depicted in Fig. 12, at the peak corresponding to the first and second mode when current is present.

4.3. Short-term response from wind and swell waves without current

The bridge motion and force responses from long-crested and short-crested wind and swell wave are summarized as standard deviations and extreme values in Figs. 16 and 17.

4.3.1. Case with long-crested wind waves

It is clear from the box plots that the variation in the response standard deviations for all 10 tests vary less than the maxima at any specific location — although they both show the same variation along the bridge girder. Focusing on the motion responses first, there are two

Table 7
Normalized standard deviation of selected pontoon motion responses when subjected to a 10000-year swell wave condition with and without 1-year current. The response ratio is given as the wave and current responses divided by the waves only responses. Both waves and current are propagating at an angle of 220° from North.

Parameter	Unit	Value			Parameter	Unit	Value		
U_c	(m/s)	0.00	1.00		U_c	(m/s)	0.00	1.00	
H_s (target)	(m)	0.46	0.46		H_s (target)	(m)	0.46	0.46	
H_s (meas.)	(m)	0.47	0.47		H_s (meas.)	(m)	0.47	0.47	
T_p	(s)	13.80	13.80	Ratio	T_p	(s)	13.80	13.80	Ratio
XPOS1	(m)	0.305	0.307	1.01	YPOS1	(m)	2.740	2.343	0.86
XPOS2	(m)	0.277	0.266	0.96	YPOS2	(m)	3.370	2.814	0.84
XPOS3	(m)	0.322	0.311	0.97	YPOS3	(m)	3.423	2.791	0.82
XPOS4	(m)	0.320	0.310	0.97	YPOS4	(m)	3.077	2.452	0.80
XPOS5	(m)	0.316	0.307	0.97	YPOS5	(m)	2.593	2.042	0.79
XPOS6	(m)	0.272	0.264	0.97	YPOS6	(m)	2.211	1.767	0.80
XPOS7	(m)	0.258	0.227	0.88	YPOS7	(m)	2.025	1.664	0.82
XPOS8	(m)	0.251	0.217	0.86	YPOS8	(m)	1.863	1.553	0.83
XPOS9	(m)	0.243	0.216	0.89	YPOS9	(m)	1.526	1.281	0.84
XPOS10	(m)	0.190	0.160	0.84	YPOS10	(m)	0.977	0.815	0.83
Average				0.93	Average				0.82
ZPOS1	(m)	0.526	0.536	1.02	PITCH1	(deg)	1.527	1.281	0.84
ZPOS2	(m)	0.822	0.833	1.01	PITCH2	(deg)	2.038	1.655	0.81
ZPOS3	(m)	0.868	0.884	1.02	PITCH3	(deg)	2.316	1.839	0.79
ZPOS4	(m)	0.857	0.878	1.02	PITCH4	(deg)	2.321	1.820	0.78
ZPOS5	(m)	0.790	0.813	1.03	PITCH5	(deg)	2.188	1.707	0.78
ZPOS6	(m)	0.783	0.791	1.01	PITCH6	(deg)	1.972	1.528	0.77
ZPOS7	(m)	0.791	0.806	1.02	PITCH7	(deg)	1.757	1.368	0.78
ZPOS8	(m)	0.755	0.782	1.04	PITCH8	(deg)	1.557	1.207	0.78
ZPOS9	(m)	0.647	0.674	1.04	PITCH9	(deg)	1.418	1.095	0.77
ZPOS10	(m)	0.394	0.404	1.03	PITCH10	(deg)	1.313	1.017	0.77
Average				1.02	Average				0.79

NB: Values are normalized w.r.t. the standard deviation of the measured wave elevation, i.e. one fourth of the listed H_s (meas.) values.

Table 8
Standard deviation of selected girder and stay-cable force responses when subjected to a 10000-year swell wave condition with and without 1-year current. The response ratio is given as the wave and current responses divided by the waves only responses and the cable tension forces are given as the average value for each set. Both waves and current are propagating at an angle of 220° from North.

Parameter	Unit	Value			Parameter	Unit	Value		
U_c	(m/s)	0.00	1.00		U_c	(m/s)	0.00	1.00	
H_s (target)	(m)	0.46	0.46		H_s (target)	(m)	0.46	0.46	
H_s (meas.)	(m)	0.47	0.47		H_s (meas.)	(m)	0.47	0.47	
T_p	(s)	13.80	13.80	Ratio	T_p	(s)	13.80	13.80	Ratio
FX END1	(N)	8.25E+04	8.15E+04	0.99	MX END1	(Nm)	9.34E+08	8.30E+08	0.89
FX HB2	(N)	3.63E+05	3.71E+05	1.02	MX HB2	(Nm)	1.52E+08	1.27E+08	0.84
FX FB2	(N)	5.62E+05	5.34E+05	0.95	MX FB2	(Nm)	5.60E+08	4.99E+08	0.89
FX FB5	(N)	6.64E+05	6.33E+05	0.95	MX FB5	(Nm)	2.35E+08	2.23E+08	0.95
FX FB7	(N)	1.01E+06	9.23E+05	0.91	MX FB7	(Nm)	5.14E+08	4.39E+08	0.85
FX END2	(N)	1.24E+06	1.18E+06	0.95	MX FB9	(Nm)	4.24E+08	3.63E+08	0.86
Average				0.96	Average				0.88
FY END1	(N)	4.25E+06	3.81E+06	0.90	MY END1	(Nm)	4.50E+06	3.95E+06	0.88
FY HB2	(N)	4.22E+06	3.78E+06	0.90	MY HB2	(Nm)	1.26E+07	1.29E+07	1.02
FY FB2	(N)	1.33E+06	1.29E+06	0.97	MY FB2	(Nm)	4.33E+07	4.13E+07	0.95
FY FB5	(N)	2.41E+06	2.06E+06	0.86	MY FB5	(Nm)	4.99E+07	4.78E+07	0.96
FY FB7	(N)	1.53E+06	1.36E+06	0.89	MY FB7	(Nm)	5.76E+07	5.52E+07	0.96
FY END2	(N)	2.75E+06	2.36E+06	0.86	MY END2	(Nm)	8.46E+07	8.37E+07	0.99
Average				0.90	Average				0.96
FZ END1	(N)	4.18E+07	3.37E+07	0.81	MZ END1	(Nm)	1.59E+07	1.30E+07	0.82
FZ END2	(N)	3.39E+07	2.66E+07	0.78	MZ HB2	(Nm)	7.34E+07	6.13E+07	0.83
Average				0.80	MZ FB2	(Nm)	4.98E+07	4.10E+07	0.82
CB 12	(N)	1.82E+06	1.53E+06	0.84	MZ FB5	(Nm)	4.84E+07	4.09E+07	0.84
CB 15	(N)	1.91E+06	1.67E+06	0.87	MZ FB7	(Nm)	3.89E+07	3.14E+07	0.81
CB 18	(N)	2.08E+06	1.95E+06	0.94	MZ FB9	(Nm)	1.62E+07	1.32E+07	0.81
Average				0.88	Average				0.82

NB: Values are normalized w.r.t. the standard deviation of the measured wave elevation, i.e. one fourth of the listed H_s (meas.) values.

distinct trends in the vertical X motion and horizontal Y motion in the local bridge girder coordinate system. The vertical motion is restrained by the tower stay-cables, resulting in the incremental increase in the response from END1 to the first pontoon. After this point, the vertical motion is somewhat constant for most of the floating bridge section, except for an increase in the dynamic response close to END2. The horizontal Y motion instead shows an 'M' shape along the bridge girder with the lowest extreme values between pontoon four and five (BY4 5) and the largest extreme values close to the first pontoon.

The force responses linked to the horizontal motion of the bridge girder are the horizontal shear force FY, the strong axis bending moment MX and the torsional moment MZ. Again, it is clearly shown that the MX and MZ moments are zero at END2 corresponding to the modelled boundary conditions. The averaged maximum in the horizontal

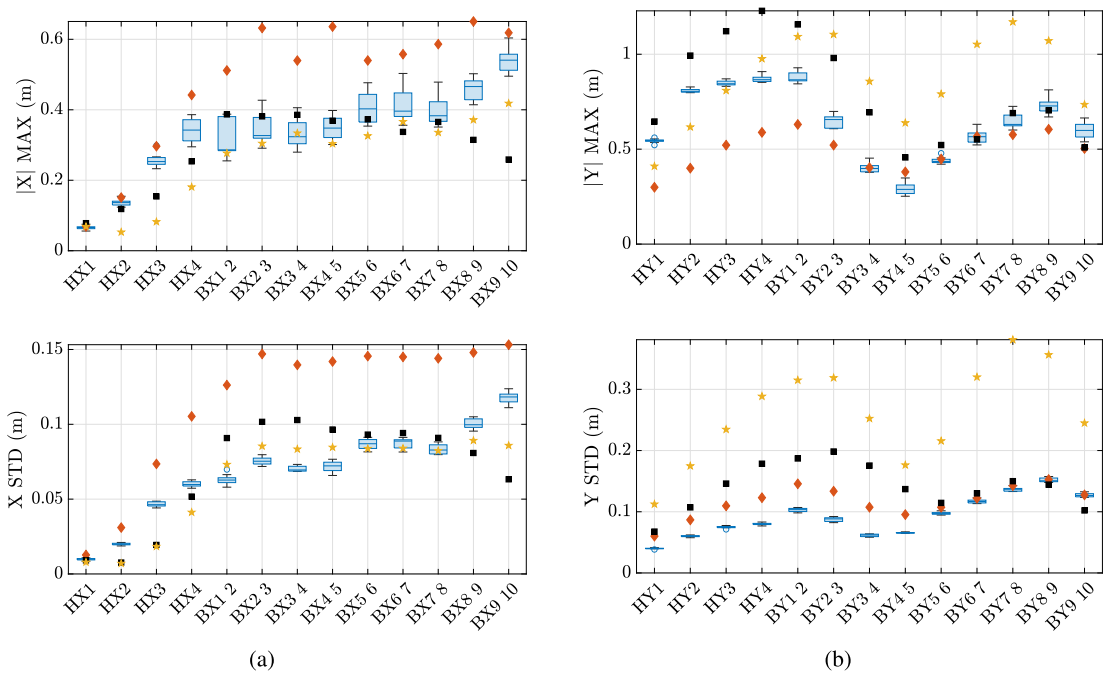

Fig. 16. Bridge girder motion responses along the bridge from 100-year wind and 10000-year swell waves propagating at a 220 degree angle from North without current. The different response types are (a) vertical motion in local girder coordinate system, and (b) horizontal motion in local girder coordinate system. Results from long-crested wind waves are depicted as blue boxplots of maxima and standard deviation, based on 10 wave tests with different wave seed numbers. From inside and out, the boxplots depict the median, the upper and lower quantiles, the minimum and maximum values (which are not outliers) and any existing outliers. Other results are shown as ♦ for short-crested wind waves, ■ for long-crested swell waves and ★ for short-crested swell waves.

shear force and strong axis bending moment both seem to fluctuate along the bridge without showing any clear tendencies. Instead, the vertical shear force FX and the weak axis bending moment MY show a very clear increase in both averaged standard deviations and maxima going from END1 towards END2 along the bridge. Both response types show the same variation along the bridge girder with a rise in the response values along the stay-cable section, a slight variation along the floating bridge section and with the largest response at END2 due to the fixed boundary condition. The relatively low values at the stay-cable section is due to the tower stay-cables restricting the vertical motion. The torsional moment MZ along the bridge girder shows the same relatively low response at the stay-cable section, due to the restriction from the cables. Directly after the last cable, the torsion response has a sharp increase at FB1, where the largest averaged maximum is found. Hereafter the averaged maximum and standard deviation fluctuate slightly while maintaining a downwards trend towards END2 where the response is zero according to the modelled boundary condition. The fact that the vertical and torsional responses are restricted by the tower stay-cables is again supported by the measured cable tension forces at the tower. Here it is clear from the standard deviations that a significant portion of the response is from the dynamic interaction between the cables and the rest of the bridge. The reason why the averaged maxima does not show the same trend is due to the static pre-tension of the cables included in the tension responses.

4.3.2. Case with long-crested swell waves

The responses from the 10000-year swell waves are generally lower than those of the wind waves, except for the bridge girder horizontal Y motion, which is expected since most of the wave energy is in the vicinity of the first two structural modes dominated by motion in the horizontal plane. The fact that most of the responses can be linked to these two mode is also clear from the significantly lower vertical shear force FX and weak axis bending moment MY responses. Although the girder horizontal shear force FY is lower when compared to wind waves, the force response show a must clearer behaviour along the bridge, which corresponds to the fact that fewer structural modes are at play.

4.3.3. Effect of directional distribution in waves

Comparing the short-crested waves to the long-crested waves for the 100-year wind condition, the forces are significantly increased. This is particularly true for the vertical shear forces FX and the corresponding weak axis bending moments MY along the bridge. This behaviour is also observed in the corresponding vertical bridge girder X motion. This result is somewhat unexpected as Langen and Sigbjörnsson (1980) have shown that a design based on long-crested waves is more conservative than one based on short-crested waves. However, their study was performed on a curved floating bridge with a continuous pontoon instead of discrete pontoons as in the present study. In the case of short-crested waves, it is expected that the pontoons will be directly excited by wave loads in the XPOS direction, which will increase the vertical and pendulum motion of the pontoon columns and thereby increase the vertical shear forces and weak axis bending moments.

For the swell wave condition the same general effect from the directional distribution of the waves is observed in the force responses. The vertical motion of the bridge girder is somewhat reduced while the standard deviations of the horizontal girder motion are significantly increased.

5. Conclusion

An experimental study of the wave- and current-induced global responses has been presented for a truncated section of the Bjørnafjord phase 5 K12 concept.

The dynamic characteristics of the bridge is captured as response amplitude operators (RAOs) via several regular wave tests and long-crested, broad-banded waves with and without collinear currents from two opposing directions roughly perpendicular to the bridge longitudinal direction.

From the pure wave tests, it was found that the axial tension of the stay-cables on either side of the bridge showed asymmetrical behaviour in the RAOs for periods between the first and second structural mode. This difference is thought to be a result of concurrent vertical and torsional motion of the bridge girder at this frequency range, resulting

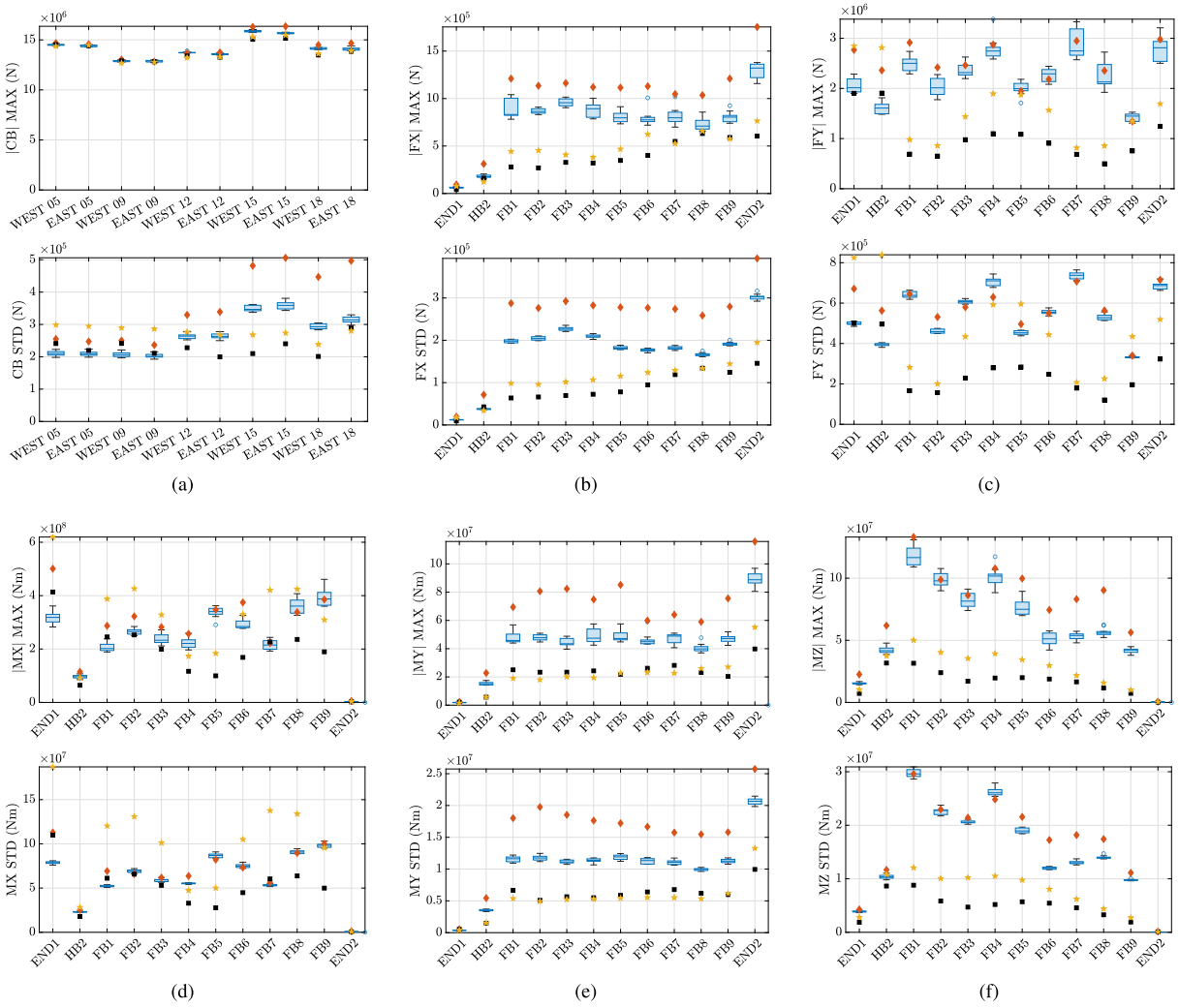

Fig. 17. Stay-cable and bridge girder force and moment responses at selected locations along the bridge from 100-year wind and 10000-year swell waves propagating at a 220 degree angle from North without current. The different response types are (a) stay-cable axial force, (b) vertical shear force, (c) horizontal shear force, (d) strong axis bending moment, (e) weak axis bending moment and (f) torsional moment. Results from long-crested wind waves are depicted as blue boxplots of maxima and standard deviation, based on 10 wave tests with different wave seed numbers. From inside and out, the boxplots depict the median, the upper and lower quantiles, the minimum and maximum values (which are not outliers) and any existing outliers. Other results are shown as ♦ for short-crested wind waves, ■ for long-crested swell waves and ★ for short-crested swell waves.

in relatively large vertical motion at one side of the girder, while the other side has significantly less vertical motion.

Non-linear wave response was observed in the responses related to horizontal motion of the bridge for wave periods close to the first two natural periods of the structure.

Collinear current was observed to have a significant influence on the responses from both 100-year wind and 10000-year swell wave conditions, which corroborated previous findings in the literature, stating that wave–current-interaction effects should be properly accounted for in the design. The current was generally observed to reduce the pontoon motion responses related to horizontal motion of the bridge, while the vertical pontoon motions were amplified – most so during the wind wave condition. For the long-crested swell waves, a reduction in almost all responses was observed – excluding a relatively small increase in the vertical pontoon motion responses.

Accounting for the directional distribution in the waves was observed to have a significant effect on the short-term responses of the bridge. For the 100-year wind wave condition, short-crested waves were observed to give larger bridge girder vertical motion and force responses than that of long-crested waves. This effect was also seen in the tension of the tower stay-cables. For the 10000-year swell wave conditions the directional distribution of the waves was observed to have the same effect on the force and moment responses while the vertical and horizontal motions of the bridge girder were, respectively, slightly reduced and slightly increased.

CRediT authorship contribution statement

Thomas Viuff: Data curation, Formal analysis, Investigation, Validation, Visualization, Writing – original draft. **Senthuran Ravinthrakumar:** Data curation, Funding acquisition, Investigation, Validation, Writing – review & editing. **Ole David Økland:** Investigation, Methodology, Project administration, Resources, Supervision, Validation, Writing – review & editing. **Ole Anton Grytå:** Resources, Supervision. **Xu Xiang:** Conceptualization, Investigation, Methodology, Supervision, Validation, Writing – review & editing.

Declaration of competing interest

The authors declare that they have no known competing financial interests or personal relationships that could have appeared to influence the work reported in this paper.

Data availability

Data can be shared upon request and agreement with The Norwegian Public Roads Administration.

Acknowledgements

The presented work was performed by SINTEF Ocean as part of the Floating Bridge Hydrodynamic Model Tests Project for the NPRA under contract 20/105662-22. The authors greatly appreciate the permission from the NPRA to publish the experimental description and results.

Funding

This work was supported by the Research Council of Norway, through SFI BLUES, grant number 309281.

References

Aarsnes, J.V., Stansberg, C.T., Reed, K., 1990a. Modellforsøk med flytebru: Enkelt pongtong. Report No. MT40 F89-0239, MARINTEK, Trondheim, Norway.

Aarsnes, J.V., Stansberg, C.T., Reed, K., 1990b. Modellforsøk med flytebru: Kontinuerlig pontongbru. Report No. MT40 F89-0252, MARINTEK, Trondheim, Norway.

AMC, 2019. Preferred Solution, K12 - Main Report. SBJ-33-C5-AMC-90-RE-100, Statens vegvesen, Oslo, Norway, https://vegvesen.brage.unit.no/vegvesen-xmlui/handle/11250/2659842.

Baarholm, G.S., 2017. Model Tests for Bjørnafjorden Floating Bridge Concept. Report No. OC2017F-176, SINTEF Ocean, Trondheim, Norway.

Cheng, Z., Gao, Z., Moan, T., 2018. Hydrodynamic load modeling and analysis of a floating bridge in homogeneous wave conditions. Mar. Struct. 59, 122–141. http://dx.doi.org/10.1016/j.marstruc.2018.01.007.

Cheng, Z., Svangstu, E., Gao, Z., Moan, T., 2019. Field measurements of inhomogeneous wave conditions in bjørnafjorden. J. Waterw. Port Coast. Ocean Eng. 145 (1), 05018008. http://dx.doi.org/10.1061/(ASCE)WW.1943-5460.0000481.

Dai, J., Abrahamsen, B.C., Viuff, T., Leira, B.J., 2022. Effect of wave-current interaction on a long fjord-crossing floating pontoon bridge. Eng. Struct. 266, 114549. http://dx.doi.org/10.1016/j.engstruct.2022.114549.

Dai, J., Leira, B.J., Moan, T., Kvittem, M.I., 2020. Inhomogeneous wave load effects on a long, straight and side-anchored floating pontoon bridge. Mar. Struct. 72, 102763. http://dx.doi.org/10.1016/j.marstruc.2020.102763.

DNV, 2010. DNV-RP-C205 Environmental Conditions and Environmental Loads. Det Norske Veritas, Oslo, Norway.

Faltinsen, O.M., 1990. Sea Loads on Ships and Offshore Structures. Cambridge University Press.

Fenerci, A., Kvåle, K.A., Xiang, X., Øiseth, O., 2022. Hydrodynamic interaction of floating bridge pontoons and its effect on the bridge dynamic responses. Mar. Struct. 83, 103174. http://dx.doi.org/10.1016/j.marstruc.2022.103174.

Langen, I., Sigbjörnsson, R., 1980. On stochastic dynamics of floating bridges. Eng. Struct. 2 (4), 209–216. http://dx.doi.org/10.1016/0141-0296(80)90002-4.

Løken, A.E., Oftedal, R.A., Aarsnes, J.V., 1990. Aspects of hydrodynamic loading and response in design of floating bridges. In: Second Symposium on Strait Crossings. Trondheim, Norway, pp. 479–486.

Moan, T., Eidem, M.E., 2020. Floating bridges and submerged tunnels in Norway - the history and future outlook. In: Wang, C.M., Lim, S.H., Tay, Z.Y. (Eds.), WCFS2019. Springer, Singapore, pp. 81–111. http://dx.doi.org/10.1007/978-981-13-8743-2_5.

Morison, J., Johnson, J., Schaaf, S., 1950. The force exerted by surface waves on piles. J. Pet. Technol. 2 (05), 149–154. http://dx.doi.org/10.2118/950149-G.

Orcina, 2018. OrcaFlex Documentation. Orcina, https://www.orcina.com/webhelp/OrcaFlex/Default.htm. (Accessed 20 February 2022).

Ravinthrakumar, S., Alsos, H., Økland, O.D., Lie, H., Xiang, X., Grytå, O.A., Kristiansen, T., 2023. Forced motion of a floating bridge pontoon to evaluate the hydrodynamic damping properties. Appl. Ocean Res. (submitted for publication).

Rodrigues, J.M., Økland, O., Fonseca, N., Leira, B., Alsos, H.S., Abrahamsen, B.C., Aksnes, V., Lie, H., 2020. Design and verification of large Floating Coastal structures: Floating bridges for fjord crossings. URL: https://onepetro.org/ISOPEIOPEC/proceedings-pdf/ISOPE20/All-ISOPE20/ISOPE-I-20-1307/2249567/isope-i-20-1307.pdf, ISOPE-I-20-1307.

Rodrigues, J.M., Viuff, T., Økland, O.D., 2022. Model tests of a hydroelastic truncated floating bridge. Appl. Ocean Res. 125, 103247. http://dx.doi.org/10.1016/j.apor.2022.103247.

Shao, Y., Xiang, X., Liu, J., 2019. Numerical investigation of wave-frequency pontoon responses of a floating bridge based on model test results. In: International Conference on Offshore Mechanics and Arctic Engineering, Vol. 1. http://dx.doi.org/10.1115/OMAE2019-96545, Offshore Technology; Offshore Geotechnics.

SINTEF Ocean, 2021a. RIFLEX 4.20.2 Theory Manual. SINTEF Ocean, Trondheim, Norway.

SINTEF Ocean, 2021b. SIMO 4.20.2 Theory Manual. SINTEF Ocean, Trondheim, Norway.

SINTEF Ocean, 2022. Sima Documentation. SINTEF Ocean, https://sima.sintef.no/doc/4.4.0/sima/index.html. (Accessed 20 February 2022).

Statens vegvesen, 2018. MetOcean Design basis. SBJ-01-C4-SVV-01-BA-001, Oslo, Norway, https://vegvesen.brage.unit.no/vegvesen-xmlui/handle/11250/2676915.

Viuff, T., 2020. Uncertainty Assessment of Wave- and Current-Induced Global Response of Floating Bridges - A Numerical Investigation (Ph.D. thesis). Norwegian University of Science and Technology, Trondheim, Norway, URL: https://hdl.handle.net/11250/2651104.

Viuff, T., Ravinthrakumar, S., Økland, O.D., Grytå, O.A., Xiang, X., 2023. Model test of a hydroelastic truncated floating bridge with a stay-cable tower. Appl. Ocean Res. 135, 103539. http://dx.doi.org/10.1016/j.apor.2023.103539.

Viuff, T., Xiang, X., Øiseth, O., Leira, B.J., 2020. Model uncertainty assessment for wave- and current-induced global response of a curved floating pontoon bridge. Appl. Ocean Res. 105, 102368. http://dx.doi.org/10.1016/j.apor.2020.102368.

Watanabe, E., 2003. Floating bridges: Past and present. Struct. Eng. Int. 13 (2), 128–132. http://dx.doi.org/10.2749/101686603777964810.

Xiang, X., Løken, A., 2019. Hydroelastic analysis and validation of an end-anchored floating bridge under wave and current loads. In: Proceedings of the 38th International Conference on Offshore Mechanics and Arctic Engineering. pp. 1–9. http://dx.doi.org/10.1115/OMAE2019-95114.

Xiang, X., Løken, A., 2020. SBJ-32-C5-SVV-21-RE-003-0 Floating Bridge Hydrodynamic Model Tests Specification 3 – High Bridge Tests. Statens vegvesen Report.

Xiang, X., Svangstu, E., Nedrebø, Ø., Jakobsen, B., Eidem, M.E., Larsen, P.N., Sørby, B., 2017. Viscous damping modelling of floating bridge pontoons with heaving skirt and its impact on bridge girder bending moments. In: International Conference on Offshore Mechanics and Arctic Engineering, Vol. 7B. http://dx.doi.org/10.1115/OMAE2017-61041, Ocean Engineering.

Xiang, X., Viuff, T., Leira, B., Øiseth, O., 2018. Impact of hydrodynamic interaction between pontoons on global responses of a long floating bridge under wind waves. In: International Conference on Offshore Mechanics and Arctic Engineering, Vol. 7A. http://dx.doi.org/10.1115/OMAE2018-78625, Ocean Engineering.